Masterarbeit
experimentell

Heat Transfer Between Particles in a Heat Recovery System for Solar Thermochemical Cycles - Experimental Investigation

Sebastian Richter

MA 105
2015-05

Lehrstuhl für Energiesysteme

Betreuer: Dipl.-Ing. Moritz Becker
Technische Universität München
Lehrstuhl für Energiesysteme
Prof. Dr.-Ing. H. Spliethoff
Boltzmannstr. 15
85748 Garching

Ausgegeben: 20.10.2014
Abgegeben: 27.05.2015

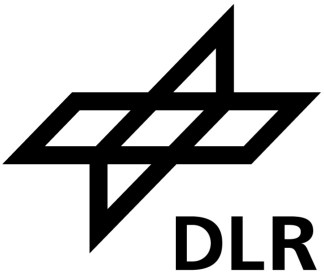

Deutsches Zentrum für Luft- und Raumfahrt e.V.
in der Helmholtz-Gemeinschaft

Betreuer: Dipl.-Ing. Jan Felinks
Deutsches Zentrum für Luft- und Raumfahrt e. V.
Institut für Solarforschung
Abteilung Solare Verfahrenstechnik
Linder Höhe
51147 Köln

Eidesstattliche Erklärung

Hiermit versichere ich, die vorliegende Arbeit selbständig und ohne Hilfe Dritter angefertigt zu haben. Gedanken und Zitate, die ich aus fremden Quellen direkt oder indirekt übernommen habe, sind als solche kenntlich gemacht. Diese Arbeit hat in gleicher oder ähnlicher Form noch keiner Prüfungsbehörde vorgelegen und wurde bisher nicht veröffentlicht.

Ich erkläre mich damit einverstanden, dass die Arbeit durch den Lehrstuhl für Energiesysteme der Öffentlichkeit zugänglich gemacht werden kann.

_____, _____ _____

Kurzfassung

Solare thermochemische Kreisprozesse zur Spaltung von Wasser oder Kohlenstoffdioxid setzen die Einbindung von Wärmerückgewinnung voraus, um deutliche Effizienzsteigerungen zu erreichen. In der vorliegenden Arbeit werden Kreisprozesse betrachtet, die partikelförmige Redoxmaterialien verwenden. Simulationen eines Systems auf Basis eines Quasi-Gegenstromwärmeübertrager und eines zweiten partikelförmigen Mediums zur Wärmeübertragung zeigten erreichbare Wärmeübertragungsraten von über 70 %. Der Mangel an wissenschaftlicher Kenntnis des Wärmeübergangs zwischen Partikeln in binären Schüttungen erfordert seine experimentelle Untersuchung. Der Wärmeübergangskoeffizient zwischen Zirkonoxid-Ceroxid-Partikeln und Aluminiumoxid-Kugeln wird in einem Teststand gemessen, die einer Stufe des vorgeschlagenen Wärmeübertragerkonzeptes entspricht. Experimente wurden für niedrige und hohe Temperaturen durchgeführt, unter Berücksichtigung verschiedener Einflussfaktoren auf den Wärmeübergang. Die Ergebnisse zeigen Werte des Wärmeübergangskoeffizienten von maximal 260 $\frac{\mathrm{W}}{\mathrm{m^2K}}$ für Temperaturen zwischen 20 and 250 °C und Werte von bis zu 786 $\frac{\mathrm{W}}{\mathrm{m^2K}}$ im Bereich effektiver Temperaturen von 870 bis 970 °C. Eine detaillierte Messunsicherheitsanalyse wird durchgeführt, um die dem Wärmeübergangskoeffizienten beigeordneten Unsicherheiten und die Beiträge der verschiedenen Quellen zu bestimmen. Die Arbeit schließt mit einem neuen Konzeptvorschlag für einen genuinen Partikel-zu-Partikel-Wärmeübertrager im Gegenstrom.

Schlagwörter: Partikeln, Schüttschichten, Wärmeübertragung, Wärmerückgewinnung, Statistische Versuchsplanung, Messunsicherheit, Thermochemische Kreisprozesse, Wasserspaltung, Solare Kraftstoffe, Konzentrierende Solarsysteme

Abstract

Solar thermochemical cycles for water or carbon dioxide splitting require the incorporation of heat recovery for significant efficiency improvements. In the present work, cycles using particulate redox materials are considered. Simulations of a system using a quasi-countercurrent heat exchanger in combination with a second particulate heat transfer medium revealed achievable heat recovery rates of higher than 70 %. The lack of scientific knowledge about heat transfer between particles in binary packed beds necessitates its experimental investigation. The heat transfer coefficient between zirconia-ceria particles and alumina spheres is measured in a test stand realizing one stage of the proposed heat exchanger concept. Experiments were conducted for low and high temperature ranges regarding different influencing factors on the heat transfer. The results show values for the heat transfer coefficient of maximum 260 $\frac{\mathrm{W}}{\mathrm{m^2K}}$ for temperatures between 20 and 250 °C, and values of up to 786 $\frac{\mathrm{W}}{\mathrm{m^2K}}$ in the effective temperature range of 870 to 970 °C. A detailed measurement uncertainty analysis is performed to identify the uncertainties assigned to the measured heat transfer coefficient as well as the contributions of the different sources. The thesis concludes with a new concept proposal for a genuine countercurrent particle-to-particle heat exchanger.

Key words: Particles, Packed Beds, Heat Transfer, Heat Recovery, Design of Experiments, Measurement Uncertainty, Thermochemical Cycles, Water Splitting, Solar Fuels, Concentrating Solar Systems

Contents

List of Figures

List of Tables

Nomenclature

Latin symbols

Symbol	Unit	Meaning
A	m^2	surface area
a	(varying)	half-width of probability distribution
a_+	(varying)	upper limit of probability distribution
a_-	(varying)	lower limit of probability distribution
a_L	$\frac{1}{\mathrm{K}}$	coefficient of linear thermal expansion
a_V	$\frac{1}{\mathrm{K}}$	coefficient of volumetric thermal expansion
b	–	linear regression coefficient
c_p	$\frac{\mathrm{J}}{\mathrm{kg\,K}}$	specific heat capacity
C_m	$\frac{\mathrm{J}}{\mathrm{mol\,K}}$	molar heat capacity
$\dot{C}$	$\frac{\mathrm{W}}{\mathrm{K}}$	heat capacity rate
d	m	diameter
m	–	number of repeated observations
m	kg	mass
$\dot{m}$	$\frac{\mathrm{kg}}{\mathrm{s}}$	mass flow
M	$\frac{\mathrm{kg}}{\mathrm{mol}}$	molar mass
q_i	(varying)	independent reading
$\bar{q}$	(varying)	arithmetic mean of readings
Q	J	transferred heat
$\dot{Q}$	W	heat flow
R^2	–	coefficient of determination
$\hat{R}^2$	–	adjusted coefficient of determination
s	(varying)	standard deviation (of the mean)
T	K	temperature
δT	K	temperature difference / temperature drop
$\overline{T}$	K	mean temperature
u	(varying)	standard uncertainty
U	(varying)	expanded uncertainty
v	$\frac{\mathrm{m}}{\mathrm{s}}$	flow velocity
V	m^3	volume
$\dot{V}$	$\frac{\mathrm{m}^3}{\mathrm{s}}$	volume flow rate
ΔV	m^3	subvolume
w_i	–	uncertainty weighting
x	–	mole fraction
x_i	(varying)	estimate of input quantity
X_i	(varying)	input quantity
y	(varying)	estimate of output quantity
Y	(varying)	output quantity

Greek symbols

Symbol	Unit	Meaning
α	$\frac{\mathrm{W}}{\mathrm{m^2K}}$	Heat transfer coefficient
β	$[1/K]$	Wärmeausdehnungskoeffizient
δ	–	thermal reduction extent
ε	(varying)	linear regression error term
Θ_a	°	acceptance angle
λ	$\frac{\mathrm{W}}{\mathrm{m\,K}}$	thermal conductivity
ρ	$\frac{\mathrm{kg}}{\mathrm{m^3}}$	density
τ	s	(contact) time
ϕ	–	porosity of the packed bed
ψ	–	heat recovery rate

Subscripts

Symbol	Meaning
an	analysis
av	average
CPC	compound parabolic concentrator
c	combined
co	co-current
discr	discretization
exp	experimental
E	end
EL	left end chamber
ER	right end chamber
HEX	heat exchanger
HT	heat transfer chamber
in	inlet
log	logarithmic
max	maximum
min	minimum
misc	miscellaneous
opt	optimum
out	oulet
ox	oxidized
P	particles
red	reduced
S	spheres
temp	temperature
T	top
TL	left top chamber
TR	right top chamber
V	volume averaged
weigh	weighing
∞	ambient conditions

1 Introduction

1.1 Motivation

Renewable energy sources play a major role in reducing anthropogenic green house gas emissions and air pollution and can help establishing a socially fairer access to energy. A main challenge for their further development, proliferation and potential to replace fossil and nuclear sources is the matching of final energy provision and varying demands in face of daily and seasonal fluctuations of solar irradiation. This necessitates the availability of low-cost storage technologies. One promising approach in this context is the conversion of solar energy to chemical fuels. This does not only address the storage issue, but may also contribute to a widespread deployment of solar-based energy carriers in the transportation sector. It is likely that chemical fuels will continue to be of great importance for it in foreseeable future (Meier and Sattler 2009).

An attractive path to solar fuels is the production of hydrogen with its numerous possible applications. It can be used for electricity generation in fuel cells, combusted directly or mixed with carbon monoxide to make syngas, which is further processed into various liquid hydrocarbon fuels. There are basically three routes for the production of solar hydrogen that may also be combined. The *photochemical/photobiological route* makes direct use of the solar photon energy for photochemical and photobiological processes. The *electrochemical route* deploys solar generated electricity from photovoltaic cells or solar thermal power plants to drive an electrolytic process. In the *thermochemical route*, high temperature heat from concentrated solar radiation allows to conduct various endothermic chemical reactions. Among these, the latter one theoretically offers the highest exergy efficiencies exceeding 50 % (Meier and Sattler 2009).

Promising thermochemical methods for water and carbon dioxide splitting are two-step cycles based on metal oxide redox pairs. They are using the principle of cycling the reactive metal oxide between the oxidized and the reduced state. In the first step, taking place at a high temperature level, the corresponding metal oxide is reduced to a lower-valence state while releasing oxygen. The subsequent step is performed at a low temperature level, where oxygen atoms of water or carbon dioxide are transferred and the reduced metal oxide is oxidized back to the higher-valence state. The high temperature reduction step is endothermic and requires the input of solar heat provided by concentrating devices (Agrafiotis et al. 2015). However, for the ceria cycle that is considered in the present work, thermal reduction proceeds to a certain extent; only a few percent of the bonded oxygen is actually released. High masses of the cycled metal oxide are therefore needed compared to the theoretical case of complete reduction, resulting in high thermal power demands for heating between the oxidation and the reduction temperature level. Some way of heat recovery is thus particularly deemed necessary.

Ceria has been identified as a promising redox material so far. It uses the redox pair of CeO_2/Ce_2O_3, cycled between the two temperature levels of 1000 °C and 1400 °C, respectively (Felinks et al. 2014). By adopting a heat recovery system, a part of the heat rejected from the reduced particles could be used to reheat the oxidized particles and reduce the required solar

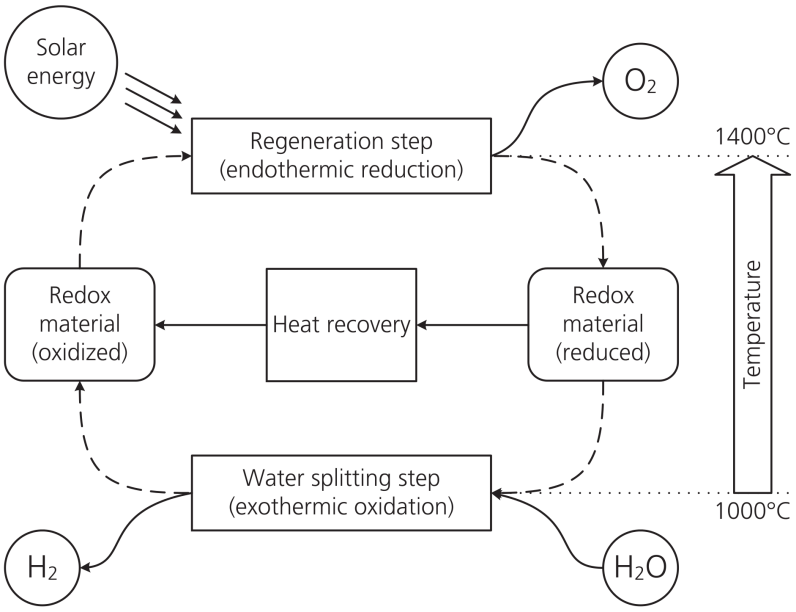

Figure 1.1: Schematic solar thermochemical cycle for water splitting including heat recovery (Felinks et al. 2014)

heat input. It was found that the use of a heat recovery system is crucial for reaching thermal efficiencies higher than 10 % (Lapp et al. 2012). Heat recovery is further of high relevance as the solar chemical plant's concentrating system accounts for approximately 50 % of its total investment cost (Steinfeld 2002). A scheme of the cycle including a heat recovery system is depicted in figure 1.1.

The proposed concept by (Felinks et al. 2014) comprises a regenerative heat exchanger system that uses solid alumina spheres as an intermediate storage medium. These are directly mixed with the redox particles for heat exchange and mechanically separated by a sieve subsequently. A simulation of this system showed the feasibility of reaching a heat recovery rate of higher than 70 % when connecting 6 mixing stages to a quasi-counter-current heat exchanger. However, for the calculation of the transferred heat, the heat transfer coefficient between redox particles and alumina spheres was estimated according to the model of (Schlünder 1984). This actually applies for the transfer from a particle bed to a wall. Using it is justified by a high diameter ratio of spheres and particles, which allows to consider the spheres' surface area as the one of a submerged wall.

In order to verify this approximation and validate the conducted simulations as well as to investigate different process parameters on the effectivity of the heat transfer, it is considered necessary to experimentally study the heat transfer characteristics of the proposed concept.

1.2 Scope of Work

A test stand for the experimental investigation of the heat transfer between ceria particles and alumina spheres had already been set up in preceding works. The general task within the scope

of this work was to modify and prepare the test stand and conduct the experiments in order to determine the heat transfer coefficient. This procedure includes processing and evaluation of measurement data as well as the analysis of results.

In the first place, several extensions have to be applied to the test stand before running it. This work encompasses the setup of a control and measuring program in National Instruments LabVIEW®. The designated thermocouples are to be calibrated in a temperature block calibrator and their assigned uncertainty is to be assessed. The thermocouples have to be arranged and installed. The test stand has to be adjusted for providing a homogeneous mixture between particles and spheres.

A measurement strategy shall be developed that addresses the process in each experimental run and depicts a way of how to compensate heat losses in the test stand. Finally, an uncertainty analysis shall be performed in order to evaluate the reliability of the findings. The procedure as well as the results are to be documented and presented in some suitable form.

1.3 Thesis Structure

Subsequent to this chapter at first some fundamentals are covered in chapter 2. Relevant aspects of solar concentrating systems and thermochemical cycles are given here. They are followed by brief explanations on the basic principles of designed experiments and the assessment and expression of uncertainty in measurement.

Different approaches for heat recovery from solid particles in the solar thermochemical and other contexts are presented and compared in chapter 3. This overview gives an idea of connected engineering challenges in conjunction with handling of particles at temperature levels around 1000 °C.

Focusing on the practical aspects of this work, chapter 4 starts by describing the preceding work on the test stand. It points out the procedure of calibration, instrumentation, mixture optimization and other steps needed in order to put the test stand into operation.

Chapter 5 is dedicated to the experimental strategy and its realization. Remarks on the measured heat transfer coefficient precede a specification of the different influencing factors tested for their significance on the heat transfer. The way of how experiments were conducted in the scope of this work, the results and the findings of the uncertainty analysis are presented. A reviewing discussion is located at the end of this chapter.

A new concept for a genuine countercurrent heat exchanger for particles in direct contact is outlined in chapter 6. The thesis concludes with the summary and outlook in chapter 7.

2 Fundamentals

2.1 Concentrating Solar Systems

Thermochemical processes for fuel production require temperature levels that are only achievable by the deployment of solar radiation when it is concentrated. This is mostly done by mirrors which reflect the sun rays to a receiver, where the radiative power is being absorbed and transferred (either to a heat transfer fluid or to a redox material directly). The ratio of the concentrated to the incident radiation flux per unit area is called the concentration ratio C. An increased value of C reduces the receiver surface area at constant thermal power and hence the heat losses that scale with it linearly. Concentrating solar power systems are usually classified by the shape of their concentrators. *Line focus systems* concentrate solar radiation to the focal line and are able to deliver heat on temperature levels up to 500 °C. Their most common application is the parabolic trough plant for the generation of electricity or process heat. *Point focus systems* deflect solar radiation onto a focal point and track the sun on two axes. Only these are applicable for thermochemical cycles due to required temperatures from several hundred up to around 2000 °C (Agrafiotis et al. 2015).

Existing point focus systems are Dish systems and Central Receiver (CR) systems, see figure 2.1. The former consist of a paraboloid mirror of about 10 m width with the absorber located in its focal point mounted to an arm. As they are limited in size and thus multiple units need to be combined for large-scale production, CR systems are favored for driving solar thermochemical processes, even though Dish systems reach higher concentration ratios. They comprise a field of individually tracked mirrors, so called heliostats. These reflect sunrays to the top of a tower, where is either placed the actual plant (solar tower system) or a mirror that re-directs the rays to the receiver placed at ground level (solar tower beam-down system). In beam down systems, concentrated solar radiation is introduced vertically into the receiver compared to approximately horizontally in conventional solar tower systems. CR systems achieve thermal power outputs of about 50 to 300 MW (Romero and Steinfeld 2012).

The concentration ratio C of point focus systems can be further boosted by incorporating non-imaging 3D-secondary concentrators, such as Compound Parabolic Concentrators (CPC). Their maximum concentration ratio is a function of their acceptance angle Θ_a (Welford and Winston 1989),

$$C_{\mathrm{CPC,max}} = \frac{1}{\sin^2(\Theta_a)} \tag{2.1}$$

assumed an ideal shape and ideal optical properties. Applications for high concentration ratios and temperatures commonly use CPCs. The equation shown above indicates that there is a trade-off between the concentration ratio and the field efficiency: A high $C_{\mathrm{CPC,max}}$ requires a narrow incident primarily concentrated beam limiting the heliostat field width. Increasing the field depth though causes a rise of radiation spillage due to mirror surface errors and an increasing mean heliostat-to-CPC distance.

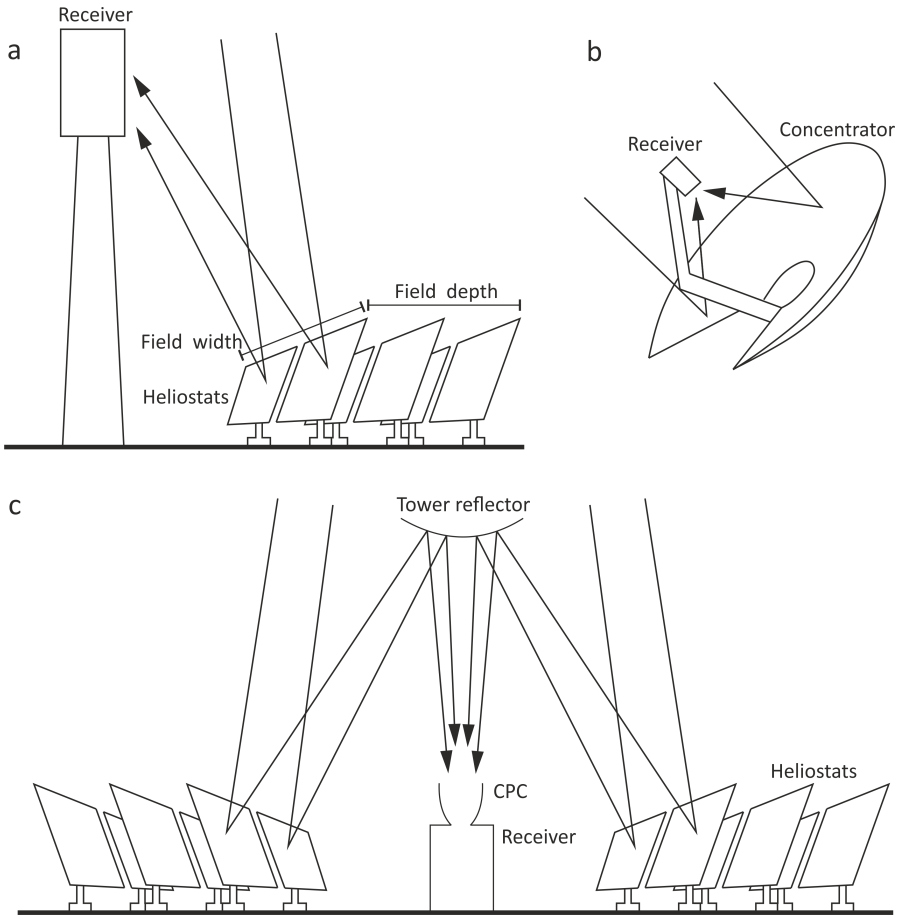

Figure 2.1: Different point focus systems: (a) Solar tower, (b) Dish system, (c) Solar tower beam-down system with secondary CPC (adapted from (Agrafiotis et al. 2015))

Within systems for solar thermal electricity generation, the receiver acts as a heat exchanger for absorbed heat to the heat transfer fluid used to drive a power cycle. In solar thermochemical processes, chemical reactions are often directly performed inside the receiver, in this context named receiver-reactor. Numerous concepts have been proposed for all the different solar thermochemical processes. Some general types of solar central receivers will be presented here.

The main category aims at the manner in which the radiative power is transferred to either the heat transfer fluid or the reactive material. Indirectly Irradiated Receivers separate the material stream from direct solar radiation by tubes that absorb the radiation and conduct it to their inside. In Directly Irradiated Receivers, also termed volumetric receivers, heat absorbing and reactive streams or structures are brought into direct contact to solar radiation that penetrates into the receiver volume (Agrafiotis et al. 2015). This can be a falling stream of solid particles or a solid foam or honeycomb structure. A further distinction is made between external and cavity-type receivers. The latter are enclosed in a casing with the radiation entering through an aperture, optionally sealed with a window. There is an angular constraint for incident radiation and the combination with a CPC is possible. A high ratio of the cavity volume to the aperture leads to a blackbody-like absorption property. This is because the unabsorbed fraction of incident radiation is primarily reflected to the inner walls rather than back to the

aperture. In contrast, external receivers are usually in the shape of cylinders with their lateral area being illuminated. These configurations show a higher re-radiation rate but may be used with circular heliostat fields. The described systems are shown schematically in figure 2.2.

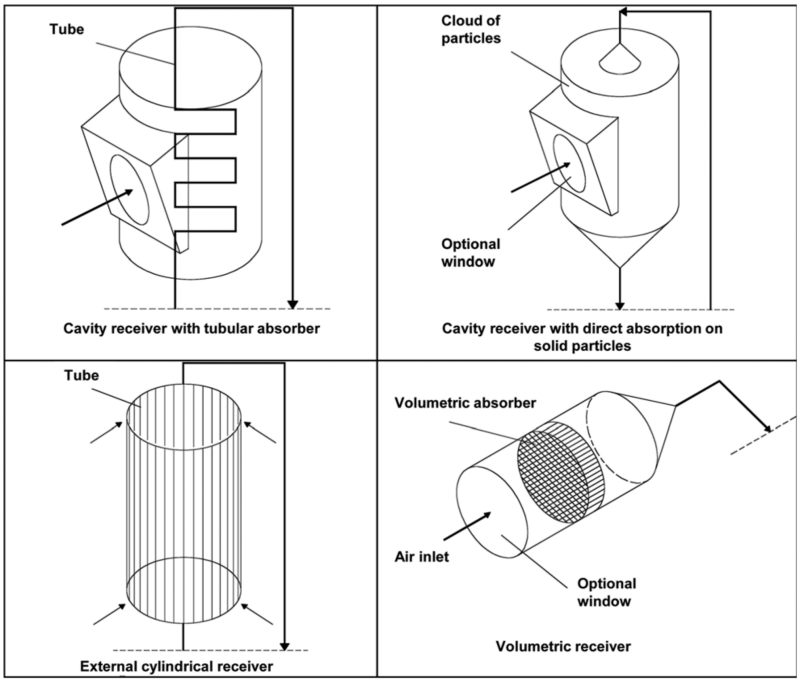

Figure 2.2: Different receiver concepts (Romero and Steinfeld 2012)

2.2 Thermochemical Redox Cycles for Water and Carbon Dioxide Splitting

In principle, an easy way of splitting water exists in its thermal decomposition, or thermolysis, in which chemical bonds are broken due to high temperature heat input (above $\sim 2500\,\mathrm{K}$). Application drawbacks of this concept are both material issues at such temperature levels and the necessity of high temperature gas separation for preventing recombination. In addition, the explosive product gas mixture induces safety issues (Steinfeld 2002).

Problematic temperature levels can be circumvented by introducing thermochemical cycles involving multiple reaction steps consecutively performed by the cycled reactive material. They take place at temperatures considerably lower than the one of the single-step thermolysis. Their net reaction yet remains the splitting reaction of H_2O to H_2 and O_2. Numerous cycles have been proposed, of which those based on metal oxides have recently been focused by research (Ermanoski et al. 2014). These are two-step processes and make use of different valence states of the employed material. During the first, endothermic high temperature regeneration step, the cycled metal oxide is reduced to the low valence state while releasing oxygen:

$$\mathrm{MeO_{ox}} \longrightarrow \mathrm{MeO_{red}} + \frac{1}{2}\mathrm{O_2} \tag{2.2}$$

The actual splitting step is taking place at a lower temperature. Here, the reduced metal oxide is oxidized back to the high valence state while it reduces water and hydrogen is released:

$$\mathrm{MeO_{red}} + \mathrm{H_2O} \longrightarrow \mathrm{MeO_{ox}} + \mathrm{H_2} \tag{2.3}$$

Due to the spatial separation of splitting and regeneration, there is no need for gas separation connected to this concept.

Indeed, for the example of the ceria cycle that is considered in this work, the given stoichiometric reactions only take place under extreme conditions. In practice, the cycle only proceeds to a certain extent; not all metal oxide material is reduced to the lower valence state but only a small percentage. This is expressed by introducing the *reduction extent* δ. The chemical equations for the ceria cycle then become:

$$\mathrm{CeO_2} \longrightarrow \mathrm{CeO_{2-\delta}} + \frac{\delta}{2}\mathrm{O_2} \tag{2.4}$$

$$\mathrm{CeO_{2-\delta}} + \delta\mathrm{H_2O} \longrightarrow \mathrm{CeO_2} + \delta\mathrm{H_2} \tag{2.5}$$

Ceria is among those cycles that require temperature for complete reduction exceeding the melting point of the redox material. This leads to various handling issues: The loss of reactive material due to vaporization and necessary shaping of re-solidified material into particles are only two examples. For that reason it is favorable to keep the reactive material in the solid state throughout the cycle (Agrafiotis et al. 2015), which though impairs the value of δ.

Another influencing factor on the reduction extent is the prevailing partial pressure of oxygen $p_{\mathrm{O_2}}$ during thermal reduction. A low value of $p_{\mathrm{O_2}}$ increases the value of δ and thus also results in an increased product yield in the splitting step. Many existing experimental setups make use of an inert purge gas to sweep the product oxygen. This method, however, implies an additional energy demand due to recycling of the inert gas with the corresponding effect on the overall process efficiency. An alternative option is the operation of the reduction step under vacuum total pressures for which beneficial effects on the reduction extent could be shown (Lange et al. 2014).

The mode of cycling the redox material between two different temperature levels is referred to as *temperature swing cycle*. In contrast, it was as well suggested to test an isothermal *pressure swing cycle* for a potential asset. However, as shown in (Ermanoski et al. 2014), this option turns out to be impractical, mainly due to steam heating energy requirement for the splitting step. Its efficiency is substantially lower than the one of the temperature swing cycle even when assuming no heat recovery at all. Processes using both pressure and temperature swing seem to be most promising.

The temperature ranges reported in literature for the ceria cycle are about $1300 - 1500\,^{\circ}\mathrm{C}$ for thermal reduction and about $900 - 1200\,^{\circ}\mathrm{C}$ for the splitting step. Optimum overall efficiencies are reached with temperature differences between reduction and oxidation of about 250 - 400 K (Ermanoski et al. 2014). Noting these values in combination with low reduction extents (causing high mass flows of cycled redox material) it is apparent that heat recovery is of overriding importance for further development of two-step thermochemical cycles. Different according concepts are presented and compared in chapter 3.

2.3 Design of Experiments

A system is defined as a combination of operations that transform input into an output with one or more observable response variables. When scientifically investigated, it is often not practically possible to describe its behavior by setting up a *mechanistic model*, which requires detailed physical knowledge about the system. In these cases, experiments can lead to an *empirical model* containing information about the performance of the investigated system and its responses to certain combinations of input factors. Besides the observation of the output response, it is essential for an experiment to deliberately change the input variables. The manner in which this is done will much affect the conclusions to be drawn from the experiment (Montgomery 2013).

There are different strategies of experimentation, of which one frequently used in practice is the *best-guess approach*. It means combining the input variables in a way of that one thinks it could lead to the desired result. It does not necessarily produce a good outcome, though, because it may require many runs and cannot guarantee that the best solution has been found. Another widely used strategy is the *one-factor-at-a-time* (OFAT) approach. Here, only one factor is successively varied over its range while the others are held constant. This approach is sometimes regarded as a "sound" scientific principle, but in fact it involves some major disadvantages. In the first place it fails to consider any possible interaction between the factors, that is, the value of one factor has an impact on the effect of another factor (and *not* on the value of the other factor). Furthermore it is less efficient than any other method based on a statistical approach to design, because it requires many test runs (Montgomery 2013).

The approach that should be used to adequately deal with interactions of several factors is the *factorial experiment*. In contrast to the OFAT-approach, the factors are varied together in this strategy and all possible combinations of the factors are used. It is easy to see that if k factors at two levels each are investigated, this method would require 2^k runs, which can quickly become infeasible with respect to time and effort. If there are four to five or more factors, it is usually unnecessary to run all possible combinations from the factorial experiment. A *fractional factorial experiment* can then be applied, using only a subset of runs and providing good information about the main factor effects as well as about their interactions.

The relationship between the varied influencing factors x_i and the response quantity y is expressed in terms of a mathematical model. This is commonly done by a multiple linear regression model (incorporating multiple input variables x_i) that is fit to the sample data (Kleppmann 2013). An example containing linear and quadratic main effects as well as two-factor interactions for a system with three factors is given by the following equation:

$$\begin{aligned} y = b_0 \; + \; & \overbrace{b_1\,x_1 + b_2\,x_2 + b_3\,x_3}^{\text{linear main effect terms}} \; + \; \overbrace{b_{12}\,x_1x_2 + b_{13}\,x_1x_3 + b_{23}\,x_2x_3}^{\text{two-factor interaction terms}} \\ & + \; \underbrace{b_{11}\,x_1^2 + b_{22}\,x_2^2 + b_{33}\,x_3^2}_{\text{quadratic main effect terms}} \; + \; \varepsilon \end{aligned} \tag{2.6}$$

The difference between the model and the measured values is expressed by the error term ε. The regression coefficients b_i, b_{ij} and b_{ii} are calculated by the least squares method, in which the sum of squared errors is minimized. In this case, the three-factor interaction term ($b_{123}\,x_1x_2x_3$) was omitted. Three-factor and higher interactions can often reasonably assumed

to be negligible. This fact is the reason why the relevant information can be won by fractional designs with a much lower number of observations. Full factorial designs provide a high number of observations that are not necessarily needed to make out the most important effects. Only a few observations are actually used to calculate the main effect coefficients or to two-factor interaction coefficients (Montgomery 2013).

In many cases a system is well characterized by a model that is linear in the factors. Nonlinear effects are frequently overestimated; in contrast, interactions play an important role in most systems and often dominate nonlinear effects (Siebertz et al. 2010).

An important assessment quantity for linear regressions is the *coefficient of determination* R^2. It relates the variability of the values predicted by the model to that of the observed values. A value of $R^2 = 1$ corresponds to a perfect congruence of observed and predicted values. The *adjusted coefficient of determination* $\hat{R}^2$ is scaled by the number of terms used in the fitting model. When adding new terms to the model, $\hat{R}^2$ only increases if the model is improved thereby. In contrast, R^2 always increases when terms are added.

The setup of a test plan for a designed experiment is done according to the rules of randomization, replication and blocking (Kleppmann 2013). Randomization means that the individual test runs are conducted in random (not arbitrary) order determined by the use of a random number generator. This procedure precludes a distortion of the result by any potential trend or unrecognized effect. Software tools for planning designed experiments are able to automatically perform this step. Replication pertains to the reduction of scatter of results and implies the repeated realization of each individual factor combination. The number of replications depends on the variance of the results and the magnitude of the effect that shall be determined. The higher the number of factors, the lower is the number of replication for each run. Blocking is a method to minimize the effect of factors that are not actually investigated, for instance different material properties of samples from different batches. If such effects are to be expected, the test plan is composed of several blocks within which the values of the disturbance factors are held constant.

Widely used test plans are those of the D-optimal type, offering a high design flexibility. They allow to include factors at different orders as well as three-factor (or higher) interactions. It is possible to freely choose the factor level values and to omit certain factor level combinations (constraints). Preceding experiments (e. g. from screening experiments) can be included in the test plan as so called inclusions. For establishing a D-optimal test plan first a full factorial design according to the chosen factors and levels is set up. A software tool is needed to select a subset from this list of run candidates by an automated algorithm in such way that the variances of the model regression coefficients are minimized (Kleppmann 2013).

2.4 Measurement Uncertainty

A thorough statement of a result that is directly measured or calculated from measured values should always contain the assigned uncertainty with regard to its correct interpretation and the assessment of its validity. In contrast to the term *error*, which is often misleading because focusing on an unknowable quantity, the term *uncertainty* expresses a doubt about

the measurement. The *Guide to the expression of uncertainty in measurement*, referred to as *GUM* (ISO/BIPM 2010), defines uncertainty as "parameter, associated with the result of a measurement, that characterizes the dispersion of the values that could reasonably be attributed to the measurand". Before the GUM was first published, uncertainties and errors were often categorized as either B-Bias or P-Precision, whose mathematical combination often resulted in unuseful final estimates of uncertainty (Ratcliffe and Ratcliffe 2015).

Falsifying influences on measurements are traditionally classified as *random effects* that arise from uncontrollable stochastic spatial and temporal variations of the measured quantity as well as quantifiable *systematic effects*. A measurement result (denoted as y) always remains an estimate of the value of the measurand Y due to random effects and to the incomplete compensation of systematic effects. Systematic effects are sometimes hard to identify; when an uncertainty is stated according the GUM, it is assumed that every effort has been made and all available knowledge has been used to identify and compensate systematic effects (ISO/BIPM 2010).

In many scientific tasks, the measurand Y is not directly measured but calculated from one or several measured quantities X_i:

$$Y = f(X_1, X_2, \ldots, X_n) \tag{2.7}$$

The functional relationship f includes all input quantities as well as corrections and correction factors where required. The input quantities X_i may themselves be measurands or depend on measured quantities and their estimates x_i are for their part assigned with uncertainties that affect the uncertainty of the measurement result y.

The uncertainty of a single measurement is combined of its several *elemental uncertainties* arising from the measured quantity itself or from the transducer used for measurement. Regardless their origin in systematic or random effects, the GUM classifies these elemental uncertainties as type A and type B. Type A uncertainties are derived from the statistical analysis of series of observations. Here, the best estimate for the measured value is the arithmetic average $\bar{q}$ of the m different readings q_i. The assigned *standard uncertainty* is estimated by calculating the experimental standard deviation of the mean:

$$s(\bar{q}) = \sqrt{\frac{1}{m\,(m-1)} \sum_{i=1}^{m} (q_i - \bar{q})} \tag{2.8}$$

It should be considered that the number m of observations is high enough in order to provide a good estimate. Choosing m too low can result in an underestimation of the standard uncertainty. In those cases, the Student's t-distribution can be used for correction.

Type B uncertainties are obtained by means other than the statistical analysis, such as previous measurement data, calibration certificates and handbooks. Just as type A ones, when type B uncertainties related to a measurement are evaluated, they should be stated as standard uncertainties for being able to consistently combine the different components. When for instance type B uncertainties are stated as multiples of a standard deviation, the multiplier is used to calculate the standard uncertainty from the given value. In other cases, a certain level of confidence can be attributed to the given uncertainty. When not stated elsewise, it can be assumed that the value is based on a normal distribution and has to be divided by the

factor corresponding to the level of confidence – 1.64, 1.96 or 2.58 for levels of 90, 95 or 99 %, respectively. There are furthermore situations where a probability of unity can be assumed for the value of the quantity to lie inside a certain interval (and a probability of zero for it to lie outside). This distribution is called even or rectangular and for instance occurs when a value is rounded or truncated. In case of a symmetric distribution the standard uncertainty is calculated according to

$$u(x_i) = \frac{a}{\sqrt{3}} \tag{2.9}$$

with a as the half width of the interval.

When the distribution of possible values within a certain interval is unknown, it is often unphysical to assume a rectangular distribution because values in the midpoint are more likely to occur. In those cases a triangular distribution with a standard uncertainty of

$$u(x_i) = \frac{a}{\sqrt{6}} \tag{2.10}$$

may be applied, where a is again the half with of the interval.

There are situations where the actual values deviate from the estimate to one side only and the estimate is not at the center of the interval. When the distances from the estimate to the upper and lower bounds are termed a_+ and a_-, respectively, the according standard uncertainty results in

$$u(x_i) = \frac{a_+ - a_-}{\sqrt{12}}, \tag{2.11}$$

assumed a rectangular distribution within the asymmetric interval.

After all elemental uncertainties u_j of a measured quantity X_i have been evaluated, they are combined to the standard uncertainty of its estimate x_i by the root sum of the squares,

$$u(x_i) = \sqrt{\sum u_j^2(x_i)}. \tag{2.12}$$

Subsequently, the standard uncertainties of the measured input quantities X_i are taken for the calculation of the *combined standard uncertainty* $u_\mathrm{c}(y)$ of the result of the calculated quantity, served by the following equation, the *law of propagation of uncertainty* (ISO/BIPM 2010):

$$u_\mathrm{c}(y) = \sqrt{\sum_{i=1}^{n} \left(\frac{\partial f}{\partial X_i}\bigg|_{x_i} \right)^2 u^2(x_i)} \tag{2.13}$$

The partial derivatives $\frac{\partial f}{\partial X_i}$ of the functional relationship from eq. 2.7, evaluated at x_i, are termed *sensitivity coefficients* as they represent the influence of a change in the respective input quantity X_i on the output quantity Y.

The combined uncertainty u_c of the result is often multiplied by a coverage factor k, which leads to the *expanded uncertainty* U defining an interval around the measurement result in which a high fraction of the distribution of values is expected to lie. The fraction of encompassed values is named the *level of confidence* p. Justified by the Central Limit Theorem, in many practical cases the probability distribution of the measurement result can be assumed to be approximately normal, even if the individual distributions are not normal. The according factors are then given as $k = 2$ for a level of confidence of 95 % and as $k = 3$ for a level of confidence of 99 %.

An important analysis procedure related to an uncertainty analysis consists in setting up reports of uncertainties, named uncertainty budgets. The uncertainty values used for propagation to the combined uncertainty are listed and compared. This allows to identify the most significant contributions as well as saving potentials, e. g. by the use of less accurate measurement equipment. The direct comparison of the individual uncertainty components is though sometimes misleading, especially for strongly differing sensitivity coefficients. A more intuitive way of comparing is enabled by calculating the weightings of the components that take into account the sensitivity coefficients,

$$w_i = \frac{\left(\frac{\partial f}{\partial X_i}\Big|_{x_i} \right)^2 u^2(x_i)}{\sum_{i=1}^{n} \left(\frac{\partial f}{\partial X_i}\Big|_{x_i} \right)^2 u^2(x_i)} = \frac{\left(\frac{\partial f}{\partial X_i}\Big|_{x_i} \right)^2 u^2(x_i)}{u_\mathrm{c}^2(y)}. \tag{2.14}$$

These can be given as percentages and easily evaluated with respect to their contribution to the combined uncertainty $u_\mathrm{c}(y)$, as it is

$$\sum_{i=1}^{n} w_i = 1. \tag{2.15}$$

3 Comparison of Heat Recovery Concepts

Heat exchangers and heat recovery systems exist in wide variety for numerous different applications. The difficulty of heat recovery in the context of thermochemical cycles arises from the fact that heat has to be exchanged between solid monolithic or particulate media. Further challenges are imposed by the necessity of pressure separation between oxidation and reduction zone. Four different reactor concepts including heat recovery published in scientific journals shall be presented here as well as common strategies used for heat recovery in other branches.

Counter-Rotating-Ring Receiver/Reactor/Recuperator Abbreviated CR5, this concept was developed by the research group of SANDIA National Labs Albuquerque, NM, USA. It is schematically shown in figure 3.1. The central unit consists of a set of rotating discs mounted on a common axis. Adjoining discs rotate in opposite direction at a rotational speed on the order of one RPM. The reactive material is arranged on the discs' outside forming rings. The reactor housing contains inlet and exhaust bores for feedstock, product and purge gases as well as the aperture assembly including a dome window. The rings are exposed to the transmitted solar radiation over a section of $\frac{1}{4}$ of their perimeter, defining the high temperature reduction zone. Oxidation takes place at the opposite $\frac{1}{4}$-perimeter section. The remaining two $\frac{1}{4}$ sections represent the heat recovery zone. Due to opposite movement of the reactive material, a countercurrent configuration is realized. Evolving product gases are swept by an inert purge gas. (Diver et al. 2010)

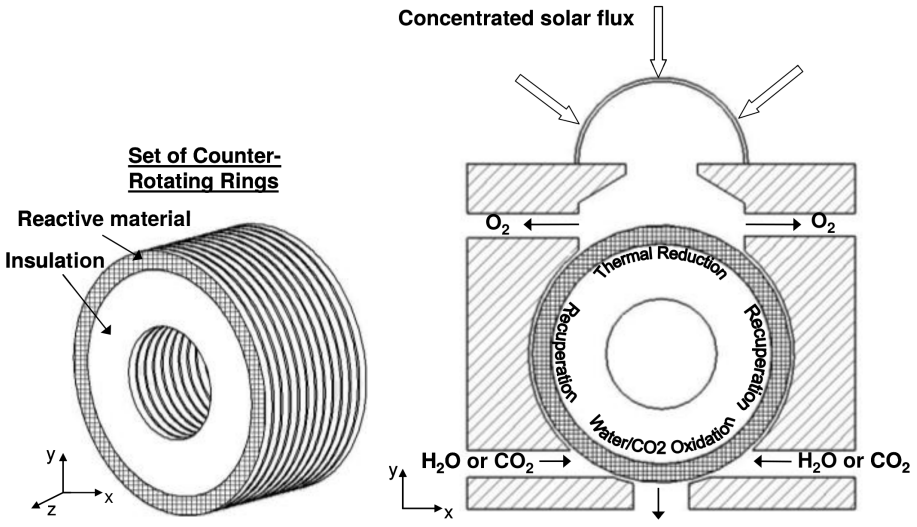

Figure 3.1: Schematic of the CR5 (not in scale) (Diver et al. 2010)

A numeric investigation of thermal states in the reactor found that the heat recovery rate achieved in the reactor is fairly low (Hogan et al. 2013). Thermal radiation is the predominant mechanism of heat transfer for recuperation. The thermal coupling between the rings is rather

weak, even at high temperatures, obviously due to disadvantegeous view factors. A significant amount of heat is lost to the housing. Figure 3.2 depicts the circumferential temperature profiles in a two-ring reactor. The temperature gain of the heated material in the heat recovery section ($\Theta = 135 \ldots 225°$) of about 60 K is very small compared to the one due to solar irradiation (about 400 K). The mechanical implementation of the counter-rotating rings is complex and induces issues of bearing and lubrication of wearing surfaces at high temperatures. Furthermore, the setup is not suitable for vacuum operation as there is no pressure separation between the oxidation and reduction reactor zone.

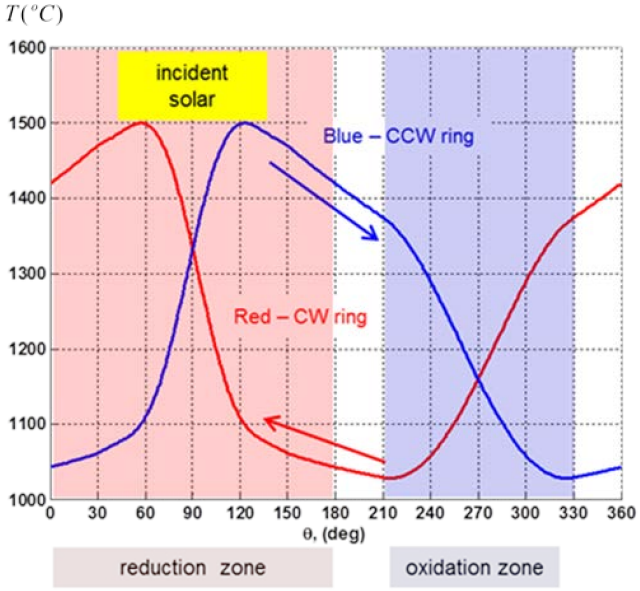

Figure 3.2: Calculated circumferential temperature distribution for two rings of the CR5 (Hogan et al. 2013)

At all, CR5 the prototype could not be tested extensively as the metal oxide structures on the rings spalled and broke and caused jamming of the drive short time after starting first operation. This example reveals a general drawback in the use of solid porous monolithic reactive structures: A low depth of penetration of solar radiation leads to high temperature gradients and stresses within the material, accompanied by the risk of disintegration.

Counter-Rotating-Cylinder Concept Another concept using rotating parts is the one suggested and investigated by (Lapp et al. 2013). It does not employ rings, but two coaxial counter-rotating cylinders, see figure 3.3. The outer – hollow – cylinder is made of a porous metal oxide structure, whereas the inner one is inert and designed for heat recovery. Similar to the concept presented before, the outer cylinder perimeter is divided into four functional sections: the preheating zone, the reduction zone, the precooling zone and the oxidation zone. Solar radiation is introduced through the aperture on the left side and illuminates the outer cylinder. The oxygen partial pressure during thermal reduction is limited by the use of purge gas.

A numerical investigation of the concept concerning temperatures, heat transfer rates and heat recovery effectiveness is conducted in (Lapp et al. 2013) in combination with a parametric

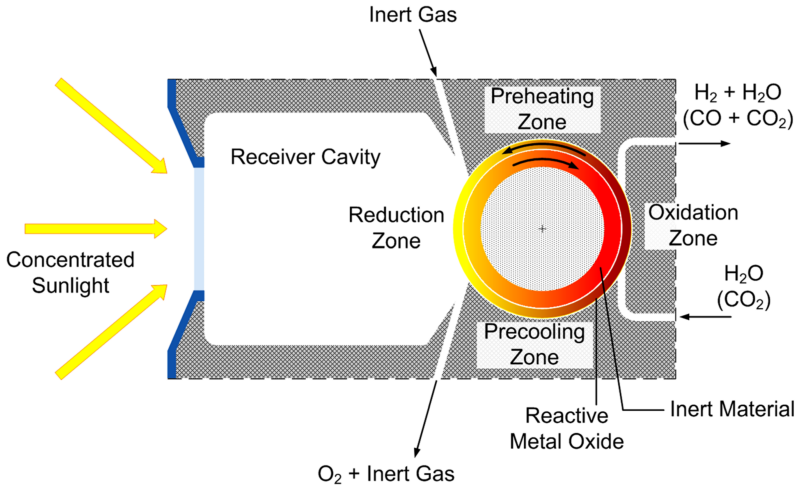

Figure 3.3: Sketch of the reactor concept using counter rotating cylinders (Lapp et al. 2013)

study. With the material properties of the considered materials (70 %-porosity ceria as the reactant, zirconia as the inert heat recovery medium), a heat recovery effectiveness of more than 50 % can be achieved. Relevant parameters were found to be the thickness of the outer cylinder and the angular frequency. An increase of the heat recovery effectiveness involved a declining maximum reactant temperature, due to the fact that the volume and the rate of cycled material, respectively, was held constant. The study does not consider interactions between the different parameters; it is thus not clear how the system behaves when changing several factors simultaneously.

There was no prototype built realizing this concept as yet. It remains questionable if the reactive one-piece cylinder can withstand circumferential and radial thermal gradients and stresses that led to a failure in the previously mentioned concept. Also, because of the porous outer cylinder, the concept is not adaptable to vacuum operation.

Moving Packed Particle Bed Reactor A path to circumvent the stability issues of monolithic reactive structures is the use of solid particles being circulated between high and low temperature reactor zones. An example is the concept of (Ermanoski et al. 2013), which employs a vertically moving packed bed of reactive ceria particles. As to be seen in figure 3.4, the outlined reactor is divided into the thermal reduction chamber (TR) and the fuel production chamber (FP). Particles at the bottom of the TR chamber are conveyed upwards by the movement of the cylindrical housing relative to a stationary conveyor auger. At the top, they are heated by vertically introduced solar radiation, perform thermal reduction and enter the vertical tube inside the auger guiding them to the fuel production chamber. Here, they are exposed to the reactant gases (H_2O and/or CO_2). Afterwards, they are conveyed back to the TR chamber by another elevator. Heat recuperation is reached by thermal conduction through the auger in the TR chamber. Descending hot particles inside the tube heat the ones moving upwards in a countercurrent mode. Beyond that, the concept comprises spatial pressure separation and thus allows vacuum operation of the TR chamber. The heat recovery effectiveness is not explicitely

evaluated in (Ermanoski et al. 2013) and is depending on the auger size. Residence times in the different chambers have to be taken into account.

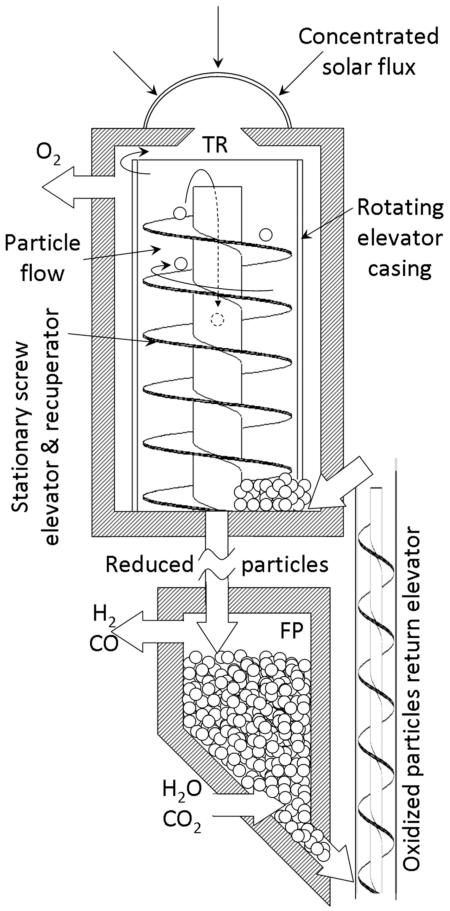

Figure 3.4: Schematic drawing of the moving packed particle bed reactor (Ermanoski et al. 2013)

However, a disadvantage remains the limited specific heat transfer between particles and auger for two reasons. The heat transfer is predominantly limited by the thermal conductivity of the packed bed. Furthermore, even if the contact surface is enhanced by the extended surface of the auger, it is much lower than the total surface area of the particles. The described concept has not been experimentally implemented and tested so far. Friction and abrasion issues remain to be observed in potential future practical implementation.

Rotary Regenerative Heat Exchangers A conceivable method of heat recovery from a stream of solid particles is the use of a rotary regenerative heat exchanger as it is applied in thermal power plants for the recovery of sensible heat of exhaust combustion gases. It consists of a structured wheel that is passed through by a cold and a hot medium simultaneously while rotating. The hot stream flows through one half of the wheel's cross section (hot channel), where heat is transferred to the wheel acting as an intermediate storage medium. In the opposite half (cold channel) heat is transmitted to the cold stream. An exemplary setup is depicted in figure 3.5.

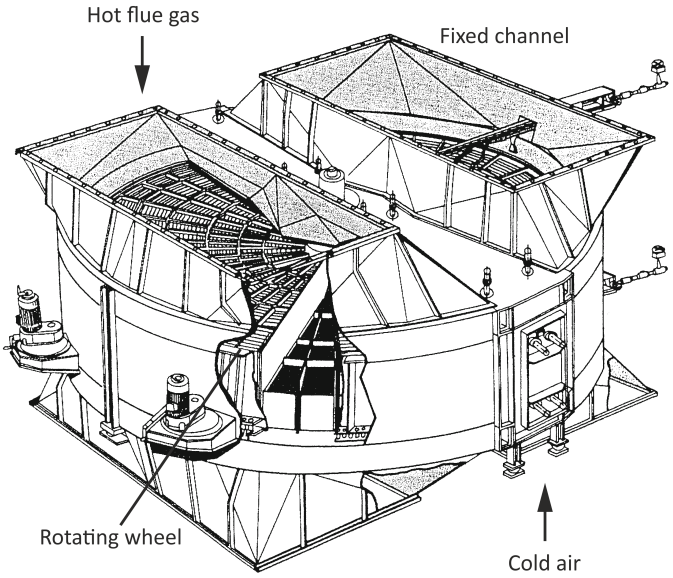

Figure 3.5: Rotary regenerative heat exchanger for power plant applications (VDI 2013)

The heat transfer performance of such systems depend to a large extent on the rotational speed of the wheel. In general the mode of operation corresponds to a cross current flow (VDI 2013). Temperature gradients over the wheel thickness tend to flatten out during residence of wheel elements in the cold entering stream. With an increasing rotational speed the axial temperature profiles of the passing streams and the wheel structure approach those of a countercurrent heat exchanger. Besides, a higher rotational speed will give rise to higher leakage between the opposite passing streams. Material is transported from the hot channel to the cold one and vice versa at the two respective edges.

Thus, this technique holds some inherent constraints when adapted to heat recovery from particulate media for thermochemical cycles. It appears to be very challenging to convey two adjacent particle streams in opposite direction through a system with not entirely sealed corresponding channels. Practically, particulate streams are conveyed at much lower speed than streaming fluids. This results in high necessary thermal capacities of the wheel as well as a very limited rotational speed, in turn constraining the countercurrent mode and the heat recovery rate. At all, a solid monolithic structure would again be integrated that has to be rotated and that is exposed to high circumferential temperature gradients at the transition of hot and cold channel. The wheel's material further has to withstand mechanical wear.

Gas-Solid Two-Phase Flow Due to their porosity, it appears favorable to recover heat from particle beds by guiding through a gas stream. A corresponding technique is applied in the cement production. The hardening component of ordinary portland cement, so called clinker, is calcinated at temperatures around 1200 °C in rotary kilns. The hot product clinker exiting the kiln is brought into contact with a stream of ambient air, commonly on pile grates in cross-flow mode. The preheated air is used for drying purposes or as combustion air in the rotary kiln (Achternbosch and Bräutigam 2000).

The realization of an optimum countercurrent operation requires a ratio of heat capacity rates of unity (Polifke and Kopitz 2011). For atmospheric operation at 1000 °C, ceria as the reactive material and nitrogen as the heat transfer fluid, the approximated volume flow ratio is

$$\frac{\dot{V}_{\mathrm{N_2}}}{\dot{V}_{\mathrm{ceria}}} = \frac{\dot{m}_{\mathrm{N_2}}}{\dot{m}_{\mathrm{ceria}}} \cdot \frac{\rho_{\mathrm{ceria}}}{\rho_{\mathrm{N_2}}} = \underbrace{\frac{\dot{C}_{\mathrm{N_2}}}{\dot{C}_{\mathrm{ceria}}}}_{=1} \cdot \frac{c_{\mathrm{p,ceria}}}{c_{\mathrm{p,N_2}}} \cdot \frac{\rho_{\mathrm{ceria}}}{\rho_{\mathrm{N_2}}} \approx \frac{0.456\ \frac{\mathrm{kJ}}{\mathrm{kg\,K}}}{1.185\ \frac{\mathrm{kJ}}{\mathrm{kg\,K}}} \cdot \frac{7400\ \frac{\mathrm{kg}}{\mathrm{m^3}}}{0.2735\ \frac{\mathrm{kg}}{\mathrm{m^3}}} \approx 10400. \tag{3.1}$$

When leading a particle stream and a gas flow in opposed direction, for instance in a tubular profile, the available effective flow cross section for the gas flow is affected by the particle bed's porosity ϕ. Beds of spherical particles exhibit a porosity of approximately 0.4 (VDI 2013). The ratio of flow velocities then becomes

$$\frac{v_{\mathrm{N_2}}}{v_{\mathrm{ceria}}} = \frac{\dot{V}_{\mathrm{N_2}}}{\dot{V}_{\mathrm{ceria}}} \cdot \frac{A_{\mathrm{ceria}}}{A_{\mathrm{N_2}}} = \frac{\dot{V}_{\mathrm{N_2}}}{\dot{V}_{\mathrm{ceria}}} \cdot \frac{1-\phi}{\phi} = 15600, \tag{3.2}$$

which is obviously impossible to be realized. The use of compressed nitrogen could in fact reduce this ratio by a factor of $\frac{p_{\mathrm{N_2}}{}'}{p_{\mathrm{N_2}}} \sim \frac{\rho_{\mathrm{N_2}}{}'}{\rho_{\mathrm{N_2}}}$ for the valid assumption of an ideal gas. Relevant compression ratios though entail high pressure handling issues, especially when looking at pressure separation for vacuum operation of the reduction chamber. Moreover, high temperature gas compression holds considerable energy penalties impairing the overall efficiency. Reducing the redox material mass flow would result in an increased heat exchanger size and affect economics.

Quasi-Countercurrent Particle-to-Particle Heat Exchanger The heat recovery concept for thermochemical cycles examined in the present work uses different particle species as both reactive material and regenerative heat transfer medium avoiding problems in connection with solid monolithic structures. It was developed in (Brendelberger et al. 2014) and (Felinks et al. 2014) and was motivated by the work of (Simonton and Stone 1986), who proposed, investigated and demonstrated a similar process for heat recovery in thermal treatment of food grain. In both concepts a hot stream of particles is mixed with a particulate heat transfer medium of different particle size. After a certain contact time for heat transfer, both particle species are mechanically separated by a sieve, see figure 3.6.

This configuration represents a co-current heat exchanger, which limits the temperature gain of the cold stream and thus impairs the heat recovery rate. The heat recovery rate is defined as the ratio of recovered heat to the maximum recoverable heat:

$$\psi = \frac{\dot{Q}_{\mathrm{HEX}}}{\dot{Q}_{\mathrm{max}}} \tag{3.3}$$

It is thus reasonable to interconnect several stages to a quasi-countercurrent heat exchanger (Brendelberger et al. 2014). The respective connection scheme is shown in figure 3.7. This setup implies a challenging process management including conveyance issues of the particle streams. Nevertheless, this design is promising as high heat recovery rates are crucial for a significant increase of the overall process efficiency.

In (Felinks et al. 2014), the quasi-countercurrent configuration was numerically investigated for high temperature operation of the ceria cycle, choosing alumina spheres as the heat transfer

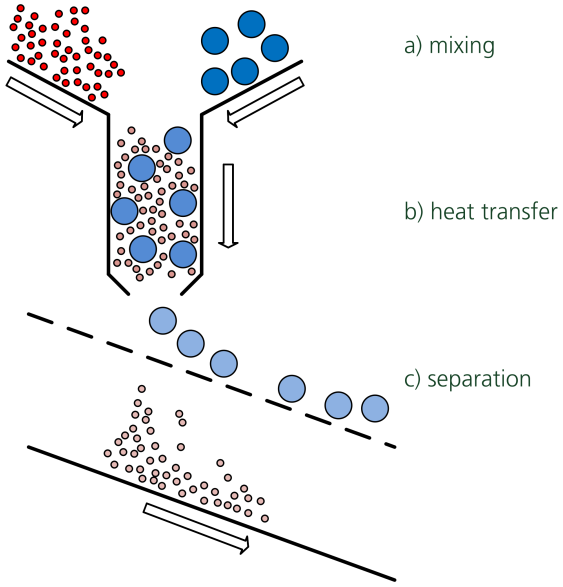

Figure 3.6: Particle flow and heat transfer in one heat exchanger stage (Felinks et al. 2014)

material. Ceria particles are hereafter just termed particles (subscript P), the spherical alumina particles of higher diameter are termed spheres (subscript S). Under consideration of temperature dependent material properties (molar enthalpy, thermal conductivity and emissivity) the heat recovery rate was calculated for varying parameters: the molar flow ratio, the contact time and the number of stages. It was found that overall heat recovery rates of higher than 70 % can be achieved with a system of six stages and a contact time in each stage of $\tau = 10\,\mathrm{s}$. A factor that had to be determined for simulation is the heat transfer coefficient between particles and spheres. (Schlünder 1984) investigated the heat transfer of packed and stirred particle beds to immersed walls on a theoretical level. The utilization of heat transfer coefficients calculated in this manner for the study of the particle heat recovery system can be justified by the different diameters of particles and spheres, regarding the total alumina surface area as that of a wall immersed in a ceria particle bed. The ratio was set to 5 in the simulation. As the heat transfer coefficient is a factor of great impact on the result of the carried out simulation, it was considered necessary to experimentally investigate the heat transfer properties between ceria particles and alumina spheres. This does in addition provide findings on the performance of the system under real-world conditions.

A proposal for a heat recovery concept using genuine countercurrent direct contact particle-to-particle heat exchangers is to be found in chapter 6.

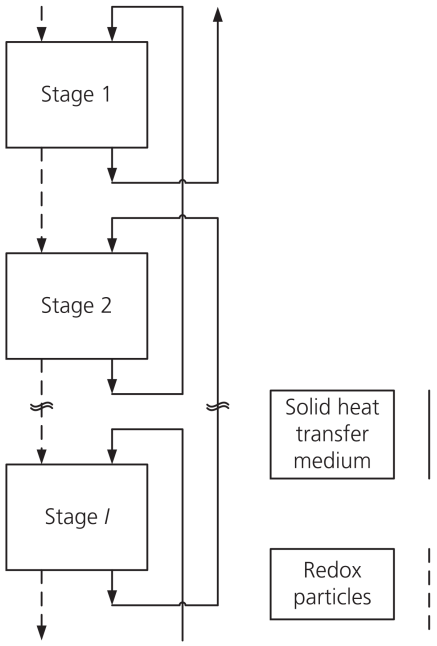

Figure 3.7: Quasi countercurrent interconnection of stages (Felinks et al. 2014)

4 Measurement Approach and Experimental Setup

The experiments within the scope of this work were conducted on a test stand that had already been set up. In this chapter at first the preceding work by Felinks will be reflected that resulted to the idea of a solid phase heat recuperation system and the conducted simulations conducted in this context. This will lead to the preliminary measurement concept setting the conditions for the test stand which had already been set up before this work was started. This chapter focuses on practical issues concerning the test stand, such as several modifications applied, establishment of the mixture and temperature measurement.

4.1 Preceding Work and Preliminary Experimental Layout

One stage of the described heat recovery concept was implemented in a lab test stand (Lachmann 2014). The heat recovery concept allows the operation of the overall thermochemical cycle in both continuous and batch mode. It was, however, regarded difficult to establish a lab-scale demonstration for continuous operation due to difficult handling of large particle amounts and questions of heat supply. The experimental setup used in this work was therefore designed for batch operation.

As mentioned in section 2.2, the use of zirconia-doped ceria with a zirconia mole fraction of $x = 0.15$ enables the enhancement of the splitting performance. After no supplier for this material could be found, particles with a zirconia mole fraction of $x = 0.84$ were chosen for investigation. Even though these values differ considerably, it is expected that useful findings for the heat transfer characteristics can be made due to similar relevant material properties of zirconia and ceria. For the heat transfer material, alumina beads ($x_{Al_2O_3} = 0.85$) were chosen. Both media were purchased from a supplier for grinding equipment.

Necessary measurands for the determination of the heat transfer coefficient are the inlet and outlet temperatures of particles and spheres, respectively. The experimental setup therefore has to automatically perform the needed steps including conveyance, mixing, separation and temperature measurement before and after in different functional chambers.

The already existing test stand consisted of several stacked blocks made of a calcium silicate solid insulation material (Promat® Promasil-1100) enclosing the chambers, see figure 4.1. The blocks are hold by metal sheets mounted on an aluminum profile frame. The two top chambers (1) contain the different species for inlet temperature measurement. They are shut and opened by inclined feeders at the bottom side, driven by linear actuators. Leaving the top chambers, spheres and particles are mixed in the mixing chamber (2), which mainly exists of a ramp of 30° inclination. The outlet of the mixing chamber leads to the heat transfer chamber (3), which is sealed by a feeder at the bottom likewise the top chambers. The mixture stays in this chamber for a defined contact time while the heat is transferred until the feeder opens and the mixture is guided to the separation chamber (4). This contains a sieve tilted by 25°, made of

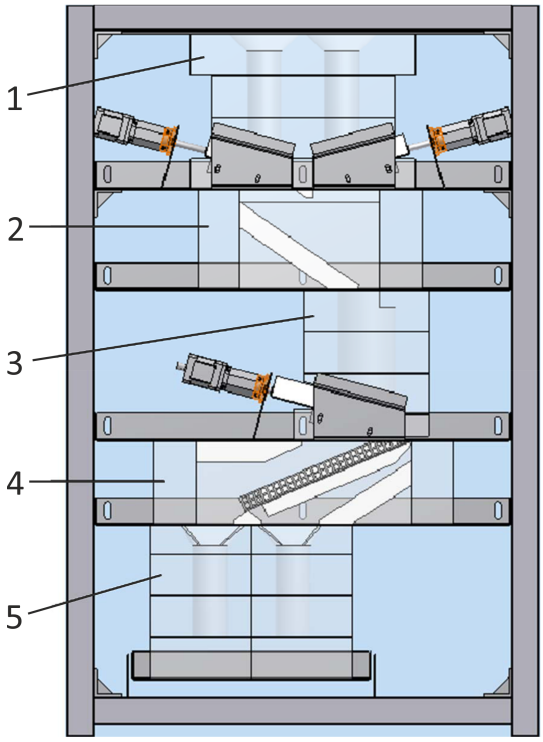

Figure 4.1: Structure of the test stand (Lachmann 2014)

high temperature resistant steel. Spheres and particles passing the sieve are supposed to fall into the end chambers (5) for outlet temperature measurement. The top chambers, the heat transfer chamber and the end chambers are of cylindrical shape.

Applied Modifications Several modifications and extensions were attached to the existing setup, such as insulation work and other modifications concerning practical handling of the test stand during experimentation. The end chambers, that were designed to be closed at their bottom were equipped with magnetically held flaps to avoid disassembly of the end chamber blocks between the experiments. The vertical feeder positions were adjusted for proper sealing of the chambers. In order to enhance conveyance on the tilted sieve and prevent blocking, a vibration motor was mounted on the separation chamber stage sheet. Control and measurement tasks were realized by LabVIEW®. A virtual instrument was programmed that allows automation of the measurement procedure (feeder movement and the vibration motor switching), monitoring and registration of measurement values. Other modifications, as mixture optimization and instrumentation are described in the respective sections 4.2 and 4.3. The modified test stand is displayed in figure 4.2.

Different influencing factors on the heat transfer coefficient were selected (Felinks et al. 2015). These are:

- diameter of particles d_P
- diameter of heat transfer spheres d_S
- mass ratio $X_\mathrm{m} = \frac{m_\mathrm{S}}{m_\mathrm{P}}$
- contact time τ (in the heat transfer chamber)

Figure 4.2: Modified test stand

- mean inlet temperature T_{in}
- inlet temperature difference of particles and spheres $\Delta T = T_{\mathrm{P}} - T_{\mathrm{S}}$
- direction of heat transfer

The procedure of how these factors were tested with respect to their influence on the heat transfer coefficient is explained in detail in chapter 5. Different combinations of some of these factors entail practical implications on the test stand. These are described in the following sections.

4.2 Mixing Procedure and Mixing Quality

For the experiments, spheres are fed into the left top chamber, particles into the right one. Both species are falling onto the ramp of the mixing chamber when the feeders of the top chambers open. They are partly mixed on the ramp and move towards the heat transfer chamber inlet. In doing so, they gain a lateral speed component due to the inclination of the ramp. The mixture bed is finally established in the heat transfer chamber.

Due to different diameters of particles and spheres and different mass ratios, the feeder positions of the top chambers had to be adapted for each combination. According to the goal to investigate the best possible performance of the overall heat recovery system, the mixture quality in the heat transfer chamber was optimized for the used experimental setup. Any homogeneous layer of particles or spheres within the mixture had to be avoided. The opaque heat transfer chamber was therefore replaced by a transparent glass tube. The filling time for both species was adjusted by the positions of the opened feeders in such manner that both streams enter the heat

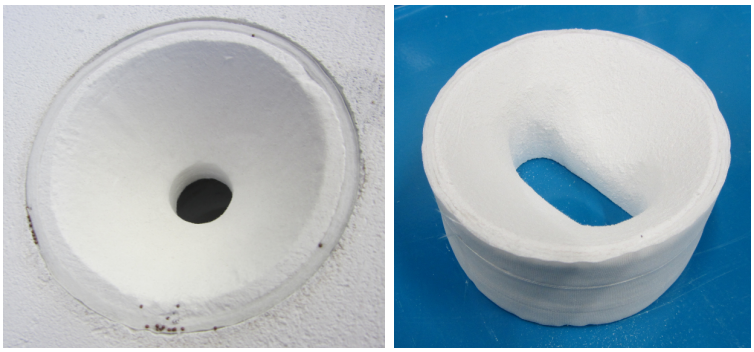

Figure 4.3: Different funnels used at the heat transfer inlet for mixture optimization, left: inserted into the heat transfer chamber

transfer chamber simultaneously with a constant flow rate in order to achieve a homogeneous concentration distribution along the chamber axis. The feeder positions differ with a changing mass ratio as well as with changing diameters of particles and spheres.

In the first mixing tests we observed a lateral inhomogeneity of particles and spheres in the chamber. The spheres are gathered on the left, the particles on the right hand side. By observing the particle motion during the filling process a separation of both species was found which may be due to the rebound on the right chamber wall. It was considered reasonable to reduce the lateral speed component of the entering particles and spheres and make them fall into the heat transfer chamber close to vertical. To reach this, the lateral opening width of the heat transfer chamber had to be decreased by the use of a funnel at the top of the heat transfer chamber. Funnels with different sizes and shapes of orifices (circular and slot-shaped) were tested, see figure 4.3.

The use of a funnel is connected to a trade-off between mixing quality and the duration of establishing the mixed bed. Smaller circular orifices showed better mixing qualities, but with unchanged feeder positions also resulted in a fill-up of the funnel during conveyance. Though, importance was attached to the limitation of the heat transfer to the heat transfer chamber due to two reasons: In the first place, the temperatures measured in the top chambers are corrected according to the results of the offset measurements (see chapter 5). A heat transfer in the filled funnel affects the actual heat transfer chamber inlet temperatures and therefore has to be minimized. Secondly, the conditions were tried to be kept as constant as possible. Varied parameters, such as mass ratio and diameters of particles and spheres could lead to a different contact time and thermal contact in the filled funnel. The top chamber feeder positions were thus adapted in such way that the funnel was not filled, which results in an increased duration of establishing the mixed bed. Moreover, the filling duration was tried to be minimized for achieving a similar residence time in the heat transfer chamber for all particles and spheres. Figure 4.4 illustrates the improvement of mixture quality by the use of the funnel.

4.3 Temperature Measurement

Thermocouples of type N were used for all temperature measurements on the experimental setup because of maximum temperatures of about 1200 °C. These are lead through the insulation

Figure 4.4: Mixture of particles and spheres in the heat transfer chamber without (left) and with the use of a funnel

material and immersed in the particle bed. Below, the calibration procedure will first be explained, followed by aspects of thermocouple arrangement and the calculation of average temperatures.

4.3.1 Calibration

Importance was attached to an accurate measurement of the temperatures. Before use, the thermocouples were therefore calibrated in a temperature block calibrator of type Isotech Pegasus Plus 1200 Site. The calibrator provides an isothermal enclosure in the form of a metal block. The to be calibrated thermometers are inserted into boreholes within the block. Their displayed temperatures are compared to those of a reference thermometer inserted into the block as well. This is a type R thermocouple annually calibrated in a certified lab in order to conduct calibrations traceable to a national standard. The setpoint calibration temperatures were approached in ascending order automatically, while all obtained temperatures were logged over time for proper identification of the periods of constant temperature. For the correction values, the values of each thermocouples was averaged over a time interval of 6 minutes was chosen in which the temperature of all inserted thermocouples was as constant as possible. The deviation of uncorrected and reference temperature was calculated for each setpoint temperature. In between the setpoints, the values are linearly interpolated which results in a piecewise linear function.

The deviations are in the range of $\pm 2\,\mathrm{K}$ and rise with the calibration temperature. The reference value is centered within the distribution, which shows that the deviation of the uncorrected thermocouples is within certain bounds and no irregularities are observed.

4.3.2 Arrangement of Thermocouples

The calculation of the heat transfer coefficient requires knowledge of the temperatures of both particles and spheres before and after heat transfer. It is practically not possible to measure these inside the heat transfer chamber where the species compose a mixture. Hence, in the

heat transfer measurements, temperatures are measured in the dedicated cylindrical top and end chambers. Here, type N thermocouples with a sheath diameter of 1.5 mm are inserted in each top and end chamber and aligned on the chamber axes at different heights, shown in figure 4.5. As one of the influencing factors, the varied mass ratio of particles and spheres leads to differing filling levels of each chamber among the experiments. The thermocouples in the top and end chambers are installed in a kind so that at least two thermocouples are immersed in the particle bed.

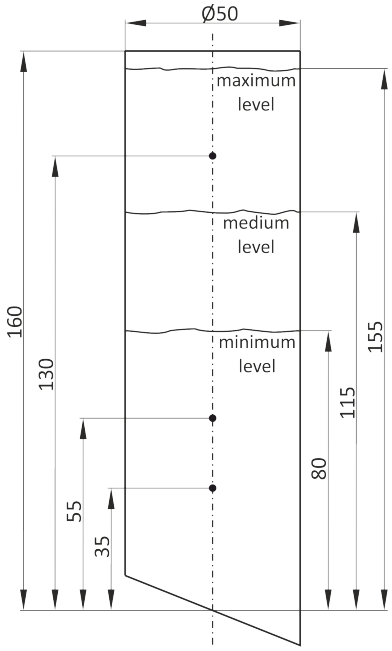

Figure 4.5: Arrangement of thermocouples in top and end chambers (all values in mm)

Due to transient heat transfer to the insulation material and heat losses to the ambiance of both particles and spheres, a deviation occurs between the temperatures measured in the top and end chambers and those actually prevailing in the heat transfer chamber at the beginning and end of the heat transfer period. These deviations had to be determined in preceding offset measurements, for which purpose the heat transfer chamber too was equipped with thermocouples of 1.0 mm sheath diameter. Once the arising deviations are obtained for different combinations of influencing factors, they can be used to calculate the actual heat transfer chamber inlet and outlet temperatures referencing the values measured in the top and end chambers. Hence, temperatures in top and end chambers have to be measured the same way in both offset measurements and heat transfer measurements.

The assimilation of the thermocouples takes a considerable amount of time. In order to minimize heat losses and to keep the temperature distribution of the particle beds in the top chambers as homogeneous as possible, the feeders were set to open before the maximum value is reached. The temperature values were taken just before feeder opening. There are no such restrictions in the end chambers, whereupon the maximum attainable temperatures were awaited and used here.

It is assumed that as a result of the mixing of particles and spheres an approximately homogeneous spatial temperature distribution is prevailing in the mixture directly after being

established in the heat transfer chamber. The best estimate for the heat transfer chamber inlet temperature needed for the offset measurements is the maximum temperature reached in the central elements in the mixture. Due to heat losses to the heat transfer chamber walls during residence in the heat transfer chamber, the temperature distribution within the mixture bed becomes inhomogeneous. The heat transfer chamber outlet temperature, again evaluated just before feeder opening, therefore has to be measured in spatial detail. It is reasonable to measure in detail the temperature gradients near the chamber walls as they are supposed to take their maximum values in this region due to heat losses to the walls. Eight thermocouples were inserted into the heat transfer chamber, their arrangement is depicted in figure 4.6.

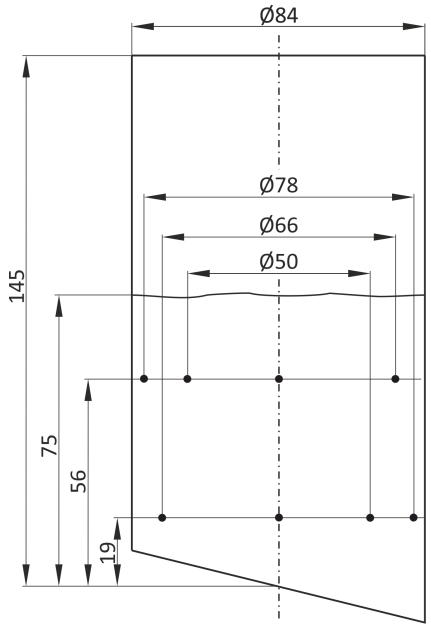

Figure 4.6: Arrangement of thermocouples in heat transfer chamber (all values in mm)

4.3.3 Average Chamber Temperatures

The temperature values obtained from the individual thermocouples are used to calculate average values for each chamber. These chamber values are used for the calculation of temperature dependent material properties and for needed temperature differences.

The arrangement of thermocouples in the chamber directly affects the way in which the average values have to be calculated. In this work, the temperatures are spatially averaged over the chamber volume. This is generally done according to the following equation (Bernhard 2004):

$$T_{\mathrm{av,V}} = \frac{1}{V} \int_V T(x, y, z)\, \mathrm{d}x\, \mathrm{d}y\, \mathrm{d}z \tag{4.1}$$

In practice, when using thermocouples, there will always be a finite number of measuring points. The volume over which the temperature is averaged is then divided into a number of subvolumes V_i, ideally of about the same size. Their boundaries are chosen to lie equidistantly

to the adjacent thermocouples. The average temperature is then obtained by the sum of each individual subvolume multiplied by the assigned temperature value:

$$T_{\mathrm{av,V}} = \frac{1}{V} \sum T_i \, \Delta V_i \tag{4.2}$$

As noted in the previous section, temperatures in the top (T) and end chambers (E) are measured by three thermocouples each that are aligned on the chamber axes. The respective mean chamber values are thus obtained by averaging over the chamber height:

$$T_{\mathrm{T/E}} = \frac{1}{h} \sum T_{\mathrm{T/E},i} \, \Delta z_i \tag{4.3}$$

In line with the offset measurements, the temperatures in the heat transfer chamber (HT) were measured in more spatial detail. The bed is divided into eight equal subvolumes, the outer ones in the form of concentric rings. Due to the same size of the subvolumes, the spatial average becomes a simple arithmetic average:

$$T_{\mathrm{HT}} = \frac{1}{8} \sum T_{\mathrm{HT},i} \tag{4.4}$$

5 Heat Transfer Quantification

5.1 Heat Transfer Coefficient

Heat transfer coefficients are predominantly used for calculus of convective heat transfer, for example for heat exchangers. According to the operation mode of the one-step particle-to-particle heat exchanger used in the present work, I will only consider co-current heat exchangers at this point. For simplicity, thermal resistances due to thermal conduction through the separating wall are neglected.

When looking at co-current heat exchangers passed through by two fluid streams and run in steady-state, the heat transfer coefficient in general varies over the run length due to different flow conditions and temperature dependent material properties. Also, as the temperature difference of the fluid streams declines with rising run length, the heat flux is a function of position, and the overall heat transfer is obtained by integration over surface:

$$\dot{Q} = \int_A \dot{q}(x)\,\mathrm{d}A = \int_A \alpha(x) \cdot (T_1(x) - T_2(x))\,\mathrm{d}A \tag{5.1}$$

In practice, when for example a heat exchanger is designed, most often a mean heat transfer coefficient obtained from empirical correlations is used to determine the heat transfer rate

$$\dot{Q} = \bar{\alpha}_x A \Delta T_{\log}, \tag{5.2}$$

where $\bar{\alpha}_x$ is averaged over surface and only valid for a special geometrical configuration. $\Delta T_{\log}$ is the logarithmic mean temperature difference.

Regarding the heat transfer between different mixed particle species in batch operation in the used test stand, the time variable supersedes the run length variable. In this case the spatial variation of the heat transfer coefficient and temperatures is either negligible or of no interest. The heat flux is then only a function of time:

$$\dot{q}(t) = \alpha(t) \cdot (T_1(t) - T_2(t)) \tag{5.3}$$

As the respective particle temperatures in a binary mixture are not practically measurable, the time dependent heat transfer coefficient is not determinable. Analogously to the previous case, a mean heat transfer coefficient can be used for the determination of the (mean) heat transfer rate:

$$\dot{Q} = \bar{\alpha}_t A \Delta T_{\log} \tag{5.4}$$

As $\bar{\alpha}_t$ is time-averaged, it is only valid for the associated contact time τ. The absolute transferred heat can thus be calculated by simple multiplication ($Q = \tau \dot{Q}$); a transformation leads to the equation the measurement concept in this work is based on:

$$\alpha = \frac{Q}{\tau A_{\mathrm{S}} \Delta T_{\log}} \tag{5.5}$$

For simplicity, the mean heat transfer coefficient averaged over τ is below just termed α (before termed $\bar{\alpha}_t$ for distinction).

The transferred heat Q can be calculated from the temperature change in either the hot or the cold particle species. Due to heat losses to the experimental setup, the value of the heat delivered by the species of higher temperature Q_{hot} is greater than the one absorbed by the species of lower temperature Q_{cold}.

$$Q_{\mathrm{hot}} = m_{\mathrm{hot}} \cdot c_{\mathrm{p,hot}} \cdot (T_{\mathrm{hot,in}} - T_{\mathrm{hot,out}}) \tag{5.6}$$

$$Q_{\mathrm{cold}} = m_{\mathrm{cold}} \cdot c_{\mathrm{p,cold}} \cdot (T_{\mathrm{cold,in}} - T_{\mathrm{cold,out}}) \tag{5.7}$$

During the experiment, heat losses are primarily due to transient heat transfer to the test stand, *i. e.* heat transfer takes place in the chamber of about room temperature. It is likely that heat losses are much lower in real-world application when the system has reached working temperature. The use of Q_{cold} for evaluation of equation 5.5 thus characterizes the performance of the present system best, but most probably leads to an underestimation of the real-world system's performance. As a compromise, Q is calculated as the average of delivered and absorbed heat:

$$Q = \frac{Q_{\mathrm{hot}} + Q_{\mathrm{cold}}}{2} \tag{5.8}$$

The total surface area A_{S} of the spheres in the mixture can be calculated as a function of the total mass of spheres m_{S}, the sphere diameter d_{S} and the density ρ_{S}. This is done by using the number of spheres n_{S} in the mixture. Primed quantities refer to a particular sphere, unprimed ones to the total amount of spheres.

$$A_{\mathrm{S}} = n_{\mathrm{S}} \cdot A'_{\mathrm{S}} = \frac{m_{\mathrm{S}}}{m'_{\mathrm{S}}} \cdot \pi\, d_{\mathrm{S}}^2 = \frac{m_{\mathrm{S}}}{\rho_{\mathrm{S}} \cdot \frac{\pi\, d_{\mathrm{S}}^3}{6}} \cdot \pi\, d_{\mathrm{S}}^2 = \frac{6\, m_{\mathrm{S}}}{\rho_{\mathrm{S}}\, d_{\mathrm{S}}} \tag{5.9}$$

The logarithmic mean temperature difference is calculated according to

$$\Delta T_{\log} = \frac{\Delta T_{\mathrm{in}} - \Delta T_{\mathrm{out}}}{\ln\left(\frac{\Delta T_{\mathrm{in}}}{\Delta T_{\mathrm{out}}}\right)} = \frac{|T_{\mathrm{S,in}} - T_{\mathrm{P,in}} - (T_{\mathrm{S,out}} - T_{\mathrm{P,out}})|}{\ln\left(\frac{T_{\mathrm{S,in}} - T_{\mathrm{P,in}}}{T_{\mathrm{S,out}} - T_{\mathrm{P,out}}}\right)}. \tag{5.10}$$

With the absolute value of the numerator positive values for $\Delta T_{\log}$ are obtained for both cases $T_{\mathrm{P,in}} < T_{\mathrm{S,in}}$ and $T_{\mathrm{P,in}} > T_{\mathrm{S,in}}$. The combined equation for the heat transfer coefficient as a function of the measurand values then results in:

$$\alpha = \frac{d_{\mathrm{S}}\, \rho_{\mathrm{S}}\, \left[m_{\mathrm{P}}\, c_{\mathrm{p,P}}\, |T_{\mathrm{P,in}} - T_{\mathrm{P,out}}| + m_{\mathrm{S}}\, c_{\mathrm{p,S}}\, |T_{\mathrm{S,in}} - T_{\mathrm{S,out}}|\right]}{12\, m_{\mathrm{S}}\, \tau\, \frac{\left|T_{\mathrm{S,in}} - T_{\mathrm{P,in}} - (T_{\mathrm{S,out}} - T_{\mathrm{P,out}})\right|}{\ln\left(\frac{T_{\mathrm{S,in}} - T_{\mathrm{P,in}}}{T_{\mathrm{S,out}} - T_{\mathrm{P,out}}}\right)}} \tag{5.11}$$

Despite the batch-wise operation of the test stand, the results for the heat transfer coefficient can be used for the prediction of a system that is run continuously. In an imaginable system where the particle mixture glides through a vertical tube the contact time is simply calculated by the tube length and the conveyance speed.

5.2 Strategy of Experimentation

The development of the temperatures of particles and spheres during a first experiment is shown in figure 5.1. The following parameters were used: $d_{\mathrm{P}} = 0.97\,\mathrm{mm}$, $d_{\mathrm{S}} = 4.95\,\mathrm{mm}$, $m_{\mathrm{P}} = 925\,\mathrm{g}$,

$m_S = 555\,g$, $T_{P,in} = 900\,°C$, $T_{S,in} = 1000\,°C$ and $\tau = 5\,s$. It is clear to see that both outlet temperatures are below both inlet temperatures, meaning both species having released heat. With this result, a proper determination of the heat transfer coefficient is impossible. The experiment reveals that heat losses to the test stand and to the ambiance at temperatures of interest are not just biasing the result but make it completely useless when no correction is applied.

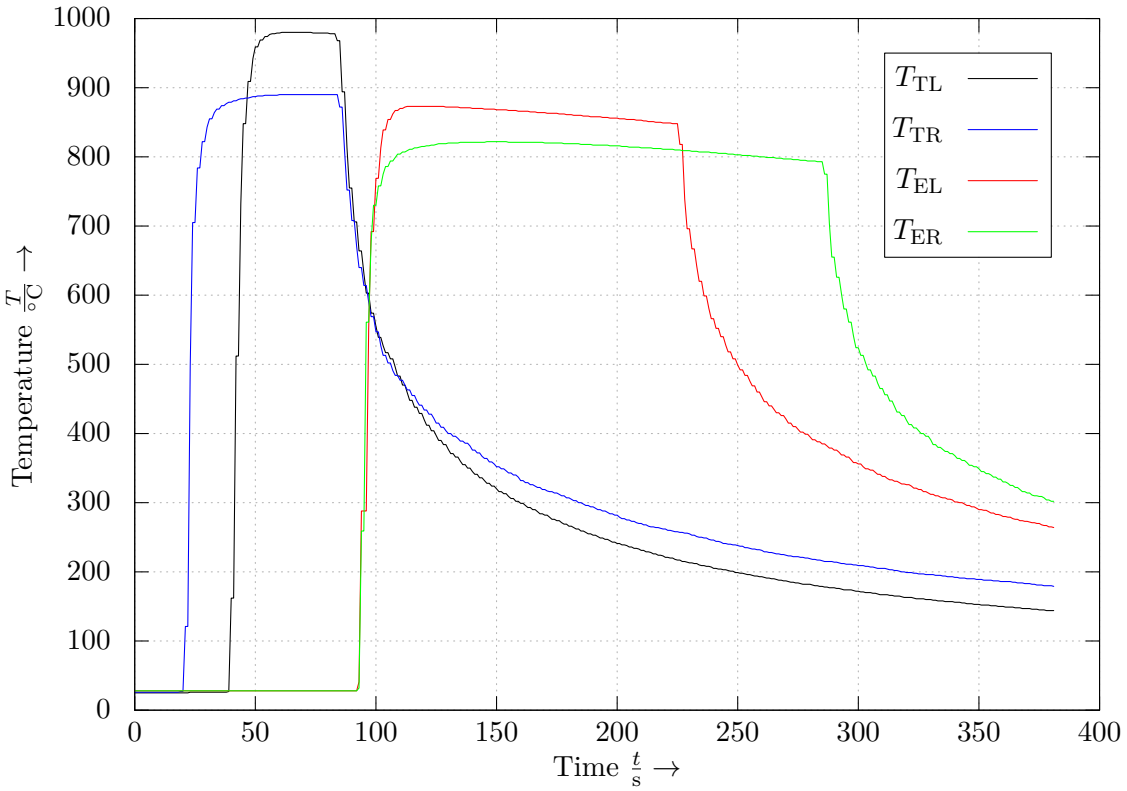

Figure 5.1: Development of chamber temperatures during a first hight temperature test run

It was for that reason decided to conduct a first experimental campaign at temperatures close to ambient temperature, further referred to as *low temperature measurements*. This procedure promised to gain experience on the test stand operation and first perceptions of the influences of the different factors.

For experiments at temperatures relevant for thermochemical cycles (termed *high temperature measurements*), a complete designed test campaign could not be conducted within the scope of this work due to lack of time. Instead, the heat transfer coefficients for some reference cases were measured. A more detailed investigation will be the subject of further studies.

For both low and high temperature measurements, an accurate calculation of the predominant heat transfer requires the quantification of heat loss induced temperature drops between top chambers, heat transfer chamber and end chambers. This was attained by separate offset measurements.

The procedure of experimental design and the selection of influencing factors for low temperature measurements, high temperature measurements and offset measurements is concretized in the following sections.

5.3 Low Temperature Measurements

Low temperature measurements were conducted in order to minimize heat losses from the particulate streams to the experimental setup. They cover the temperature range between 20 and 250 °C. Below, I will first give a more detailed description of the selected influencing factors. Subsequently, the making of the test plan will be outlined.

5.3.1 Influencing Factors

The different investigated influencing factors listed in section 4.1 are explained in more detail at this point. Their influence on the heat transfer is discussed and the reasons for selecting them and their levels are given.

Diameter of Particles d_P The heat transfer from a wall to a packed particle bed is mainly determined by two factors: The thermal resistance at the contact surface and the thermal resistance of penetration (VDI 2013). The latter one is depending on the particle bed's thermal conductivity. This will thus affect the heat transfer, when the heat transfer spheres' surface area is regarded as the one of a submerged wall (as in (Felinks et al. 2014)). The thermal conductivity of a packed bed is amongst others a function of its porosity ϕ, *i. e.* the ratio of void volume to total volume, which actually varies slightly with the particle diameter. The particle diameter was nonetheless included as an influencing factor to make out this potential effect.

It is further to be assumed that the particle diameter (as well as the sphere diameter) has an impact on the constitution of the mixture and the spatial homogeneity of the concentrations of the respective species. This itself has a significant influence on the heat transfer performance.

In potential applications, the choice of the particle diameter depends on various factors. Oxygen diffusion, questions of conveyance and the use of pressure separation beds for vacuum operation are some examples. It is thus reasonable to include different particle diameters in the investigation of the heat transfer characteristics.

Particles of $d_\mathrm{P} = 0.8, 1.0$ and $1.5\,\mathrm{mm}$ were chosen for the investigation. Smaller diameters are by trend preferable, but the chosen values promised easier handling, such as sealing the chambers.

Diameter of Spheres d_S A combination of equations 5.5 and 5.9 shows the sphere diameter's influence on the calculated heat transfer coefficient:

$$\alpha = \frac{Q\, d_\mathrm{S}\, \rho_\mathrm{S}}{6\, m_\mathrm{S}\, \tau\, \Delta T_\mathrm{log}} \tag{5.12}$$

Assumed a constant transferred heat, higher sphere diameters will rise the heat transfer coefficient as the total spheres' surface area decreases. It is to be expected that the amount of transferred heat will be reduced by higher sphere diameters leading to a compensation of this effect. However, all this does not account for high contact times: In this case, a major part of the heat will be transferred in both cases, irrespective of the sphere diameter. There is yet an effect of the contact time and the mean logarithmic temperature. For high sphere diameters, transient heat transport within the particular spheres could become relevant.

As mentioned above for the particle diameter, an effect of the sphere diameter on the homogeneity of the mixture and consequently the heat transfer can furthermore be expected.

Mass Ratio X_m The theoretical analysis of a heat recovery system based on two single stage co-current heat exchangers with an intermediate storage medium reveals an optimum ratio of absolute heat capacities. According to (Polifke and Kopitz 2011), the efficiency of a (continuously operated) co-current heat exchanger is given as:

$$\eta_\mathrm{co} = \frac{1 - \mathrm{e}^{-NTU(1+\frac{\dot{C}_\mathrm{c}}{\dot{C}_\mathrm{h}})}}{1 + \frac{\dot{C}_\mathrm{c}}{\dot{C}_\mathrm{h}}} \tag{5.13}$$

The theoretical efficiency of the above described heat recovery system is obtained by multiplying equation 5.13 by the same equation with the inverse ratio of heat capacities ($\frac{\dot{C}_\mathrm{h}}{\dot{C}_\mathrm{c}}$). The analysis of the resulting equation leads to an optimum ratio of heat capacities of unity. Transferred to the batch case this results in an optimum mass ratio:

$$\left.\frac{m_\mathrm{S}}{m_\mathrm{P}}\right|_\mathrm{opt} = \underbrace{\left.\frac{C_\mathrm{p,S}}{C_\mathrm{p,P}}\right|_\mathrm{opt}}_{=1} \cdot \frac{c_\mathrm{p,P}}{c_\mathrm{p,S}} \tag{5.14}$$

As a matter of fact this result is only valid for ideal conditions like temperature independent heat capacities and adiabatic heat exchanger walls and can thus be tested with varied mass ratios.

The mass ratio furthermore affects the mixture quality with the corresponding effect described in the preceding paragraphs. For higher mass ratios, increased direct contact between the spheres is likely to occur, hindering the heat transfer between particles and spheres.

Contact Time τ The heat transfer coefficient obtained from the measurements is averaged over the contact time, as it was shown in section 5.1, necessitating to include this factor in the investigation.

Mean Inlet Temperature $\overline{T}_\mathrm{in}$ The effect of the bed's thermal conductivity on the theoretical heat transfer coefficient has already been mentioned above. Thermal conductivity in porous media depends to a large extent on thermal radiation in the pores. As high temperature ranges in the experiments are covered, thermal radiation will also have a substantial influence on the heat transfer at the contact surface of the different species.

On account of the temperature dependent material properties as well, the mean inlet temperature is an influencing factor of particular importance.

This was achieved by the use of mean inlet temperatures of $\overline{T}_{\mathrm{in}} = 70\,\mathrm{K}$ and 150 K and inlet temperature differences of $\Delta T = 50\,\mathrm{K}$ and 100 K.

Inlet Temperature Difference ΔT Besides of its influence on the transferred heat via the logarithmic mean temperature difference, an effect of the temperature difference of particles and spheres at the entry of the heat transfer chamber on the heat transfer coefficient is investigated due to temperature dependent material properties, as stated above.

Direction of Heat Transfer A different temperature dependent emissivity of the respective materials could lead to a differing heat transfer coefficient when heat is either transferred from hot particles to cold spheres or vice versa. This factor is the only categorical factor included in the investigation.

The selected influencing influencing factors and the applied levels used for the low temperature measurements are summarized in table 5.1.

Table 5.1: Influencing factors and their levels for low temperature measurements

Factor	Symbol	Levels	Unit	Type
Diameter of particles	d_{P}	0.73, 0.97, 1.38	mm	continuous
Diameter of heat transfer spheres	d_{S}	3.76, 4.95	mm	continuous
Mass ratio	X_{m}	0.3, 0.6, 1.0	-	continuous
Contact time	τ	5, 13, 20	s	continuous
Mean inlet temperature	$\overline{T}_{\mathrm{in}}$	70, 150	°C	continuous
Inlet temperature difference	ΔT	50, 100	K	continuous
Direction of heat transfer	-	$T_{\mathrm{P,in}} > T_{\mathrm{S,in}}$, $T_{\mathrm{P,in}} < T_{\mathrm{S,in}}$	-	categorical

The chosen factor levels are not equally spaced and the number of levels differ among the factors. Using the D-optimal criterion for setting up the test plan is consequently the favorable method, compare section 2.4. The software camLine Cornerstone® was used for this purpose.

Despite the lower temperatures, first experiments still revealed substantial differences in the heat delivered by the hot species and the one absorbed by the cold species. This fact showed that the correction of the temperature values is necessary for low temperature measurements as well.

5.3.2 Offset Measurements

As stated in section 4.3.2, four temperature deviations between the different averaged chamber temperatures are to be evaluated. These are the differences between the inlet temperature in the heat transfer chamber and the outlet temperatures in the top chambers on left and on the right side, ΔT_{TL} and ΔT_{TR}, as well as the differences between the outlet temperatures in the heat transfer chamber and the inlet temperatures in the end chambers, ΔT_{EL} and ΔT_{ER}. An overview of the deviations and the notation is given in figure 5.2.

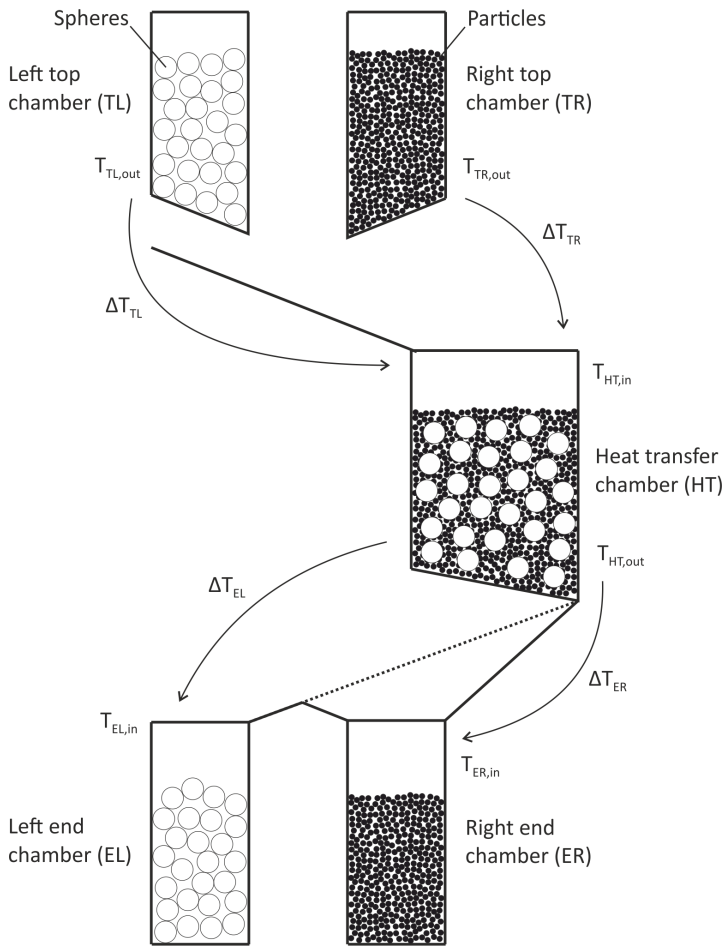

Figure 5.2: Overview of chamber temperatures and temperature drops between the chambers

$$\Delta T_{\mathrm{TL}} = T_{\mathrm{HT,in}} - T_{\mathrm{TL,out}} \tag{5.15}$$

$$\Delta T_{\mathrm{TR}} = T_{\mathrm{HT,in}} - T_{\mathrm{TR,out}} \tag{5.16}$$

$$\Delta T_{\mathrm{EL}} = T_{\mathrm{HT,out}} - T_{\mathrm{EL,in}} \tag{5.17}$$

$$\Delta T_{\mathrm{ER}} = T_{\mathrm{HT,out}} - T_{\mathrm{ER,in}} \tag{5.18}$$

ΔT_{TL} and ΔT_{TR} are thus expected to be negative, ΔT_{EL} and ΔT_{ER} to be positive.

The experimental conditions for the offset measurements need to be preferably similar to those prevailing during the low temperature heat transfer measurements. The temperature drops cannot be evaluated individually because the presence of one particulate stream affects the heat losses of the other one. All four arising temperature drops are therefore measured in the same test run.

Particles and spheres were heated to the same inlet temperature before being fed into the top chambers. This is because, first, heat transfer between the different species would falsify the measured temperature drops and, second, temperature measurement in the heat transfer chamber is only unambiguously performable for equal temperatures of particles and spheres.

Due to two different mean inlet temperatures combined with two different inlet temperature differences used in the low temperature measurements, particles and spheres exhibit eight different temperatures. Individually determining the temperature drops for each occurring temperature would lead to a number of runs double the one necessary for the low temperature measurements. The offset measurements were thus planned as a designed experiment, too. In doing so, the particle diameters, sphere diameters and mass ratios were not changed compared to the low temperature measurements. As the inlet temperature is of great impact on the absolute deviations, it is varied over three levels. The nominal absence of heat transfer between the species justifies the exclusion of the contact time, the inlet temperature difference and the direction of heat transfer from the list of factors used in the offset measurements.

As the thermocouples in the top chambers are aligned on the chamber axes, they measure the bed's core temperature. Consequently, an additional factor had to be included in order to account for transient heat losses to the top chambers. The residence time of spheres and particles in the top chambers was chosen for this purpose. The selected factors and the applied values are listed in table 5.2.

Table 5.2: Values of influencing factors for low temperature offset measurements

Factor	Symbol	Levels	Unit	Type
Diameter of particles	d_P	0.73, 0.97, 1.38	mm	continuous
Diameter of heat transfer spheres	d_S	3.76, 4.95	mm	continuous
Mass ratio	X_m	0.3, 0.6, 1.0	-	continuous
Inlet temperature	T_in	45, 147.5, 250	°C	continuous
Top chamber residence time	τ	30, 60, 90	s	continuous

5.3.3 Evaluation Procedure

A VBA macro for Microsoft Excel® was programmed for automated evaluation of the data records generated in LabVIEW®. It calculates the time dependent average chamber temperatures according to section 4.3.3, thereby automatically selecting the relevant thermocouples according to the respective mass ratio. Changes in the feeder positions are recognized and used for determining the moment of feeder opening, at which the outlet temperatures (in the top chambers and the heat transfer chamber) are evaluated. The inlet temperatures (in the heat transfer chamber and the end chambers) are evaluated by finding the maximum average values in the respective chambers.

In case of offset measurements, the average chamber temperature values are used to calculate the temperature deviations according to equations 5.15 to 5.18. Afterwards, these are inserted into the statistical analysis software (camLine Cornerstone®) performing the linear regression.

The analysis of the actual heat transfer measurements requires the knowledge of the temperatures of particles and spheres prevailing before and after contact. They are calculated according to the results of the statistical offset measurement analysis temperatures in the top chambers. The thus obtained temperatures are first used to calculate temperature dependent quantities

as the sphere diameter, the sphere density and specific heat capacities. The way of how this is done is presented below. Subsequently, the heat transfer coefficient is determined according to equation 5.11.

Temperature dependent quantities – the sphere diameter d_S, the spheres' bulk density ρ_S and the heat capacities of particles $c_{p,P}$ and spheres $c_{p,S}$ – were corrected for the respective case. The temperatures of particles and spheres were therefore approximated by the arithmetic average during the heat transfer phase,

$$\overline{T}_P = \frac{T_{P,in} + T_{P,out}}{2} \tag{5.19}$$

and

$$\overline{T}_S = \frac{T_{S,in} + T_{S,out}}{2}. \tag{5.20}$$

The distribution of particle and sphere diameters was analyzed in (Felinks et al. 2015). An image processing method using a flat bed scanner was applied to determine the sauter mean diameter, which is generally used for the characterization of particle size distributions. It is defined as the particle diameter in a hypothetical bed of identical spherical particles with a total surface area equal to the one of the real particle bed. In the following, the sphere diameter always corresponds to the sauter mean diameter.

The sphere diameter was measured at ambient temperature and was corrected depending on the temperature with respect to thermal expansion. Despite the actual thermal expansion anisotropy of alumina of about 10 % (Chikh et al. 2014), thermal expansion was assumed to be equivalent in all three spatial dimensions. The an average coefficient of linear thermal expansion of $a_L = 7 \cdot 10^{-6} \frac{1}{K}$ (Martienssen and Warlimont 2005) was used for correction. The larger effective diameter appearing during the experiments was thus estimated as follows:

$$d_S(\overline{T}_S) = d_{S,\infty}\,(1 + a_L\,\overline{T}_S). \tag{5.21}$$

The sphere's bulk density, measured with a pycnometer at ambient temperature, was corrected analogously. As the density is proportional to the reciprocal volume, which in turn is affected by the diameter, the corrected diameter was used for correction of the density.

$$\rho_S(\overline{T}_S) = \rho_{S,\infty}\frac{d_{S,\infty}^3}{d_S^3(\overline{T}_S)} = \frac{\rho_{S,\infty}}{(1 + a_L\,\overline{T}_S)^3} \approx \frac{\rho_{S,\infty}}{1 + 3\,a_L\,\overline{T}_S} \tag{5.22}$$

The approximation is justified by the fact that $a_L \ll 1$; for isotropic materials it is $3\,a_L = a_V$, with a_V as the volumetric thermal expansion coefficient.

For the low temperature measurements, a differential scanning calorimeter was used in (Felinks et al. 2015) for the measurement of the specific heat capacities of particles and spheres. The taken values were fitted with third-order polynomials in the form of

$$c_p(T) = a_1 + a_2\,T + a_3\,T^2 + a_4\,T^3 + a_5\,T^{-2} + a_6\,T^{-3}. \tag{5.23}$$

As the heat capacities could not be measured with the available calorimeter for high temperatures, they were calculated according to tabulated values. The molar heat capacities C_m of the pure components of particles (ZrO_2 and CeO_2) and spheres (Al_2O_3, MgO, SiO_2 and CaO)

were taken from (Barin 1995) and fitted individually over the relevant temperature range by fifth-order polynomials (see annex A). The molar heat capacity of the mixture cannot be given as a continuous function due to changes in the crystal structure of some components with changing temperatures.

The components' molar heat capacities were combined to the particles' and spheres' molar heat capacities,

$$C_{\mathrm{m,P}} = x_{\mathrm{ZrO_2}} C_{\mathrm{m,ZrO_2}} + x_{\mathrm{CeO_2}} C_{\mathrm{m,CeO_2}} \tag{5.24}$$

$$C_{\mathrm{m,S}} = x_{\mathrm{Al_2O_3}} C_{\mathrm{m,Al_2O_3}} + x_{\mathrm{MgO}} C_{\mathrm{m,MgO}} + x_{\mathrm{SiO_2}} C_{\mathrm{m,SiO_2}} + x_{\mathrm{CaO}} C_{\mathrm{m,CaO}} \tag{5.25}$$

with the mole fractions x_i of component i in the mixture. The specific heat capacity of particles and spheres is calculated from

$$c_{\mathrm{p,P/S}} = \frac{C_{\mathrm{m,P/S}}}{M_{\mathrm{P/S}}} \tag{5.26}$$

with $M_{\mathrm{P/S}}$ as the molar mass of particles/spheres.

5.3.4 Statistical Analysis

This section is intended to present the procedure of statistical analysis and the development and evaluation of the regression model. The procedure is illustrated with examples from the analysis; the actual results are given in section 5.3.5.

The setup of a valid regression model for a sample of data points is an iterative process. In the first place, a *step-wise regression* is performed automatically by the deployed software. It consists in an initial simple linear regression for each factor including the calculation of each respective coefficient of determination R^2 (compare section 2.3). Those factors that lead to a model with a calculated high R^2 are included. Afterwards, all factors not yet included in the model are successively tested for a positive effect on the coefficient of determination and are integrated when the effect is significant. This step is repeated until no further significant factor can be found (Kleppmann 2013). The significance of a factor is expressed in terms of its *significance value* that characterizes the probability that the respective effect is due to random effects. Low values thus indicate significance.

After this first step-wise regression has been performed, the identified factor effects are manually checked for significance and plausibility. This is facilitated by so called *adjusted response graphs* provided by the software. They separately show the effect of each included factor on the response value. Figure 5.3 exemplarily depicts the adjusted response graph for the temperature drop ΔT_{TR} from the right top chamber to heat transfer chamber after the initial step-wise regression.

Note that the plotted dots are not measured values but adjusted response values with the effects of the other effects averaged out. In this case, the most distinct effects emanate from the top chamber temperature and residence time. The particle diameter as well as the mass ratio show quadratic effects with a minimum at the central level. This trend is implausible and goes along with a high spread of residuals compared to the predicted effect. The quadratic terms for both particle diameter and mass ratio are consequently excluded from the regression. It further appears doubtful that the sphere diameter has an significant effect on the particle

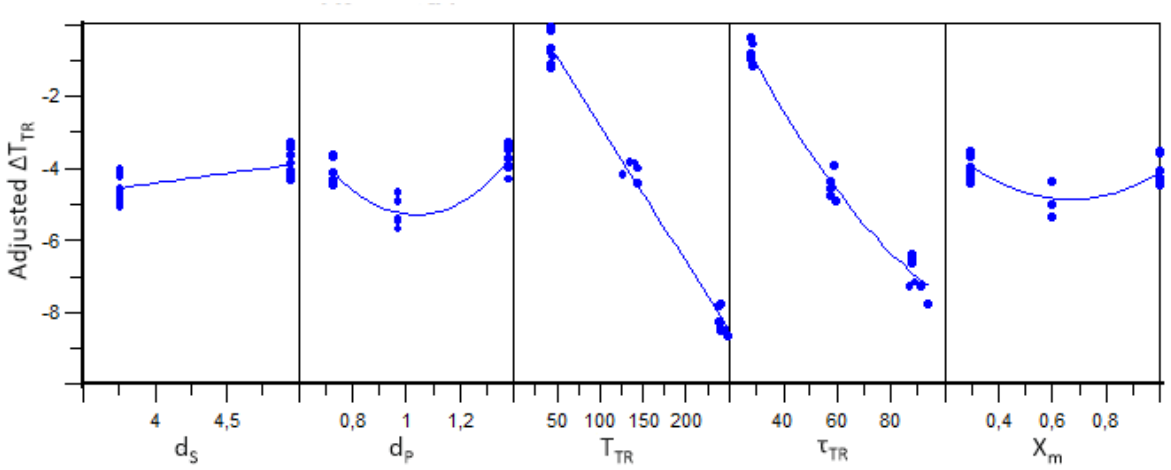

Figure 5.3: Adjusted response graph from analysis for ΔT_{TR} after first step-wise regression

temperature drop. As the predicted effect is low and afflicted with a high residual spread, it is excluded as well.

A new model exempt from the non-physical effects is then obtained by a repeated step-wise regression. The next refinement step is the test of the normal distribution of the residuals in order to check the model adequacy. For this purpose, the software provides the residuals probability plot. It shows the studentized residuals against the quantile. Residuals resembling the straight line indicate that they are normally distributed. With this plot, potential outliers can also be made out easily. Figure 5.4 shows an example for ΔT_{TL} – the rightmost dot's residual is much larger than any of the others. In fact this dot refers to a test run where there had been a sealing problem in the heat transfer chamber during measurement potentially affecting the measured temperature. Putative outliers that cannot be explained by errors in experimentation or evaluation have to be handled with care. Excluding a point from the dataset used for the regression should not be solely justified by the location in the residuals probability plot but be based on further studies (Montgomery 2013).

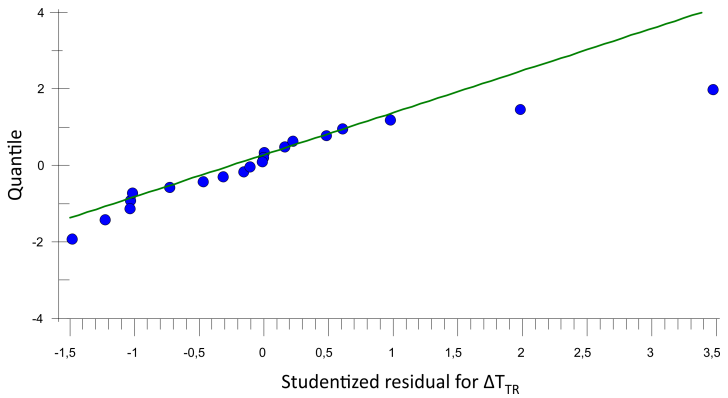

Figure 5.4: Residuals probability plot from analysis for ΔT_{TL} after first step-wise regression

For the statistical analysis of the offset measurements, all four temperature drops defined in section 5.3.2 represent a response variable. Four independent regression models are thus established here. The influencing factors are different for each particular model: Every

temperature drop is modeled as a function of the temperature measured in the respective top or end chamber. The residence time in the top chambers is moreover only relevant for the drops from the top chambers to the heat transfer chamber. The actual low temperature heat transfer measurements comprise the heat transfer coefficient α as the only response variable. The analysis procedure shown in this section is basically the same for offset and heat transfer measurements.

5.3.5 Results

Offset Measurements

Figure 5.5 depicts the residuals probability plots for the regression of each temperature drop. All residual distributions are approximately normal, the highest deviations from the straight line are found for the residuals for ΔT_{EL} indicating a possible departure from normality. Potential outliers could be identified for ΔT_{TR} and ΔT_{EL}. However, they remain included because no experimental irregularities could be made out for the corresponding data points.

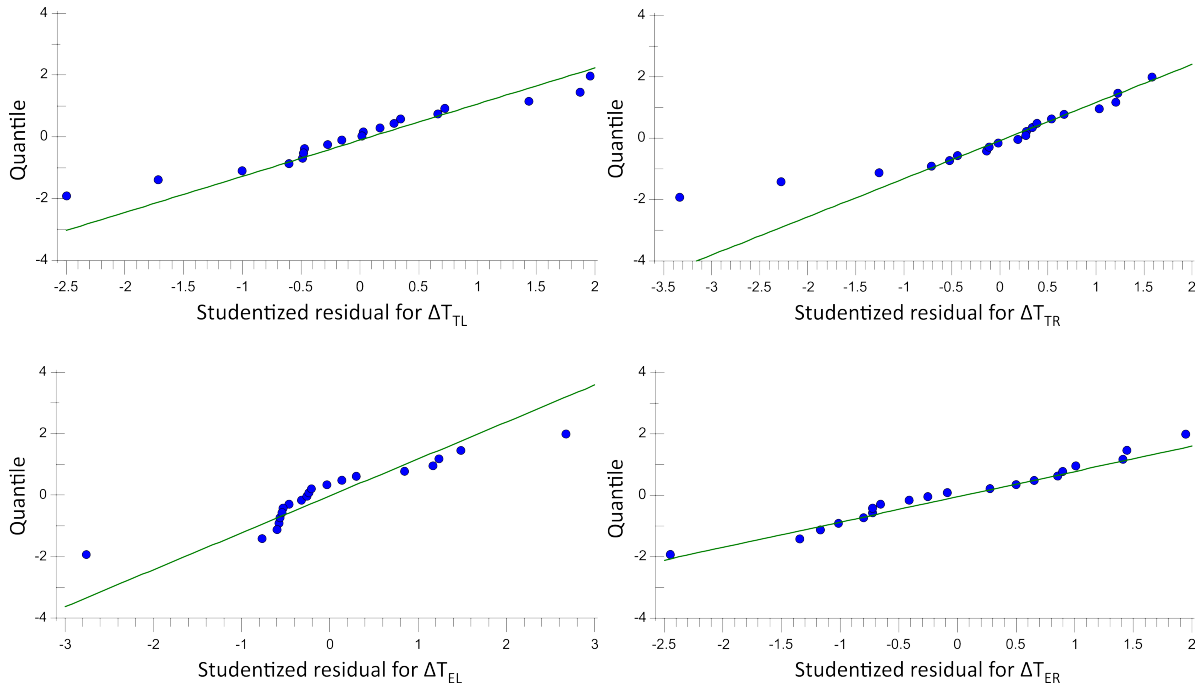

Figure 5.5: Residuals probability plots for low temperature offset measurement analyses

The resulting regression models for each temperature drop are illustrated in figures 5.6, 5.7, 5.8 and 5.9. The model for ΔT_{TL} is the only one with more than two significant factors; the diagram is therefore parametrized with X_{m} as weakest effect, resulting in multiple surface layers.

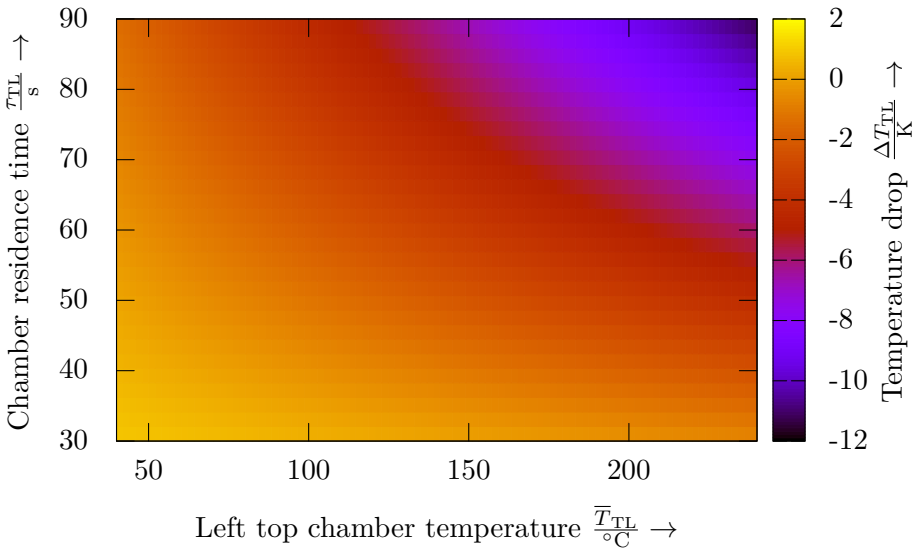

Figure 5.6: Surface response plots of regression models for ΔT_{TL}

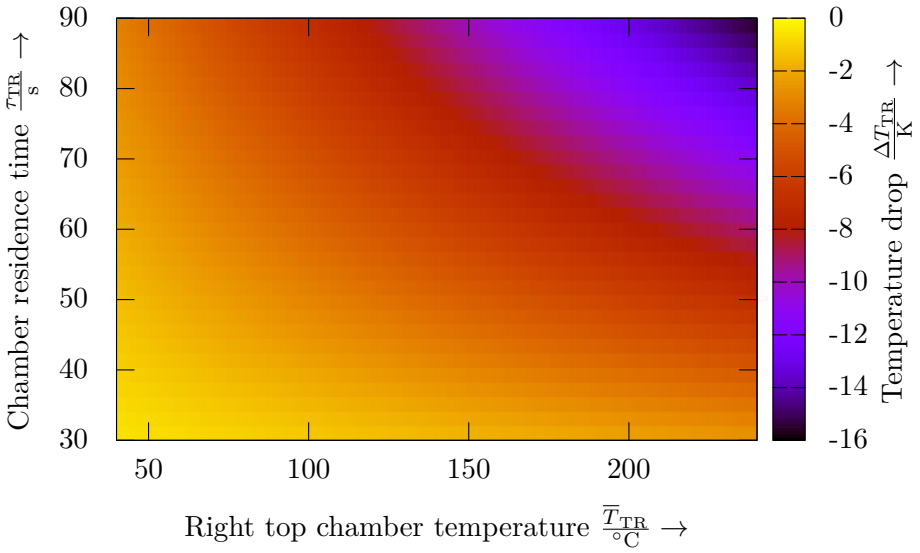

Figure 5.7: Surface response plots of regression models for ΔT_{TR}

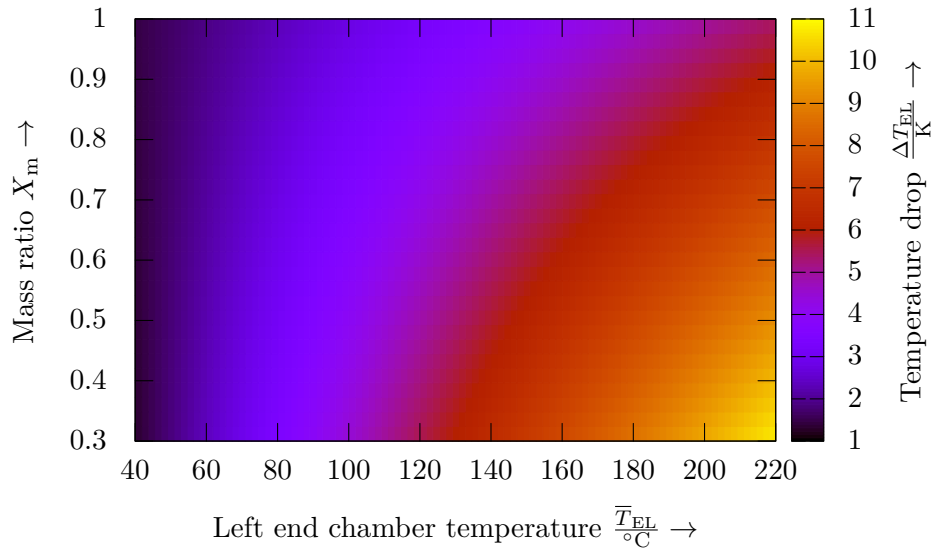

Figure 5.8: Surface response plots of regression models for ΔT_EL

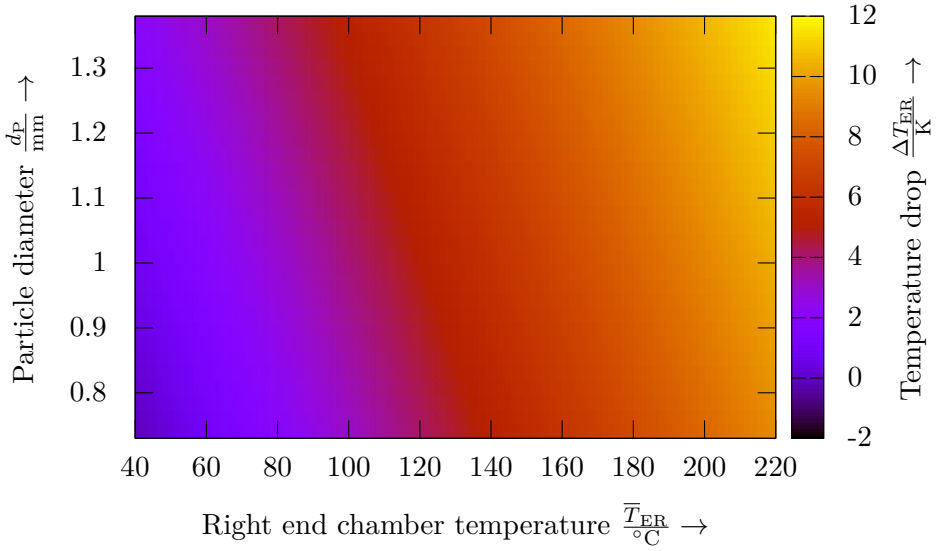

Figure 5.9: Surface response plots of regression models for ΔT_ER

No quadratic factor effects were considered for the offset measurements because they were either not plausible or automatically excluded due to low significance. The dominating effect in each case is the respective chamber temperature. It induces the strongest variations in the temperature drops. Concerning the top chambers, the temperature drops furthermore show a strong dependency on the residence times. A comprehensible effect is the interaction of both: The higher the top chamber temperature, the higher is the residence time's effect on the heat loss to the chamber walls.

The mass ratio showed a slight effect only on the sphere temperature drops ΔT_{TL} and ΔT_{EL}. Since $X_{\mathrm{m}} = \frac{m_{\mathrm{S}}}{m_{\mathrm{P}}}$, higher mass ratios correspond to higher sphere masses. For ΔT_{TL} an increased X_{m} leads to a higher temperature drop, whereas for ΔT_{EL} it leads to a lower one. This behavior is not understood, however, due to considerable significance values it was not eliminated from the model, which would have led to distinctly lower values of $\hat{R}^2$.

The sphere diameter was evaluated to have no significant influence at all. The particle diameter solely affects ΔT_{ER}.

The predicted values from the regression model comply with the following polynomial,

$$\Delta T_i = b_{0,i} + b_{1,i} \cdot d_{\mathrm{P}} + b_{2,i} \cdot X_{\mathrm{m}} + b_{3,i} \cdot T_i + b_{4,i} \cdot \tau_i + b_{5,i} \cdot T_i \cdot X_m + b_{6,i} \cdot T_i \cdot \tau_i, \qquad (5.27)$$

with i = TL, TR, EL, ER. Table 5.3 summarizes the regression coefficients for the different factors and the particular obtained coefficients of determination.

Table 5.3: Regression coefficients and adjusted coefficients of determination for low temperature offset measurements

Coefficient	Associated factor(s)	Coefficient values			
		$i = \mathrm{TL}$	$i = \mathrm{TR}$	$i = \mathrm{EL}$	$i = \mathrm{ER}$
$b_{0,i}$	-	2.786	0.1420	-1.410	-4.821
$b_{1,i}$	d_{P}	-	-	-	3.388
$b_{2,i}$	X_{m}	-2.094	-	1.976	-
$b_{3,i}$	T_i	$1.289 \cdot 10^{-2}$	$1.605 \cdot 10^{-2}$	$6.601 \cdot 10^{-2}$	$5.340 \cdot 10^{-2}$
$b_{4,i}$	τ_i	$-1.143 \cdot 10^{-2}$	$1.046 \cdot 10^{-2}$	-	-
$b_{5,i}$	$T_i \times X_{\mathrm{m}}$	-	-	$-4.424 \cdot 10^{-2}$	-
$b_{6,i}$	$T_i \times \tau_i$	$-6.885 \cdot 10^{-4}$	$-8.711 \cdot 10^{-4}$	-	-
$\hat{R}^2$		0.9500	0.9622	0.8215	0.8538

Heat Transfer Measurements

The residuals probability plot for the analysis of the heat transfer coefficient measurements is displayed in figure 5.10. The residuals follow the normal distribution well. The rightmost dot is a suggestive of an outlier. Nevertheless, since there were no experimental abnormalities observed, it was not excluded.

The only significant factors remaining after the step-wise regression are the mean heat transfer chamber inlet temperature $\overline{T}_{\mathrm{in}}$ and the contact time τ. No interaction is evaluated between

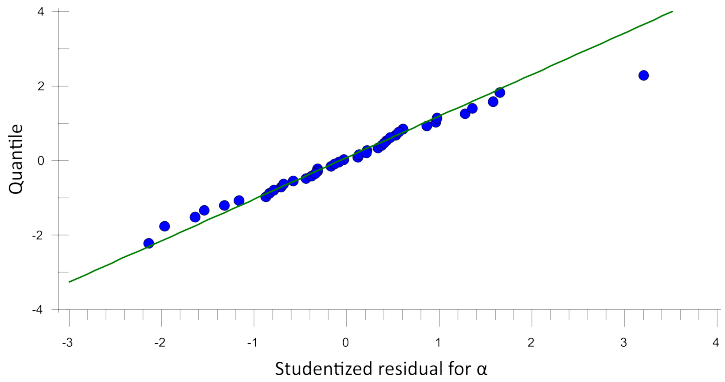

Figure 5.10: Residuals probability plots for low temperature heat transfer measurement analysis

these factors. Figure 5.11 shows the development of the heat transfer coefficient depending on the factors in a surface plot. Values for α of up to 260 $\frac{\mathrm{W}}{\mathrm{m^2\,K}}$ are reached.

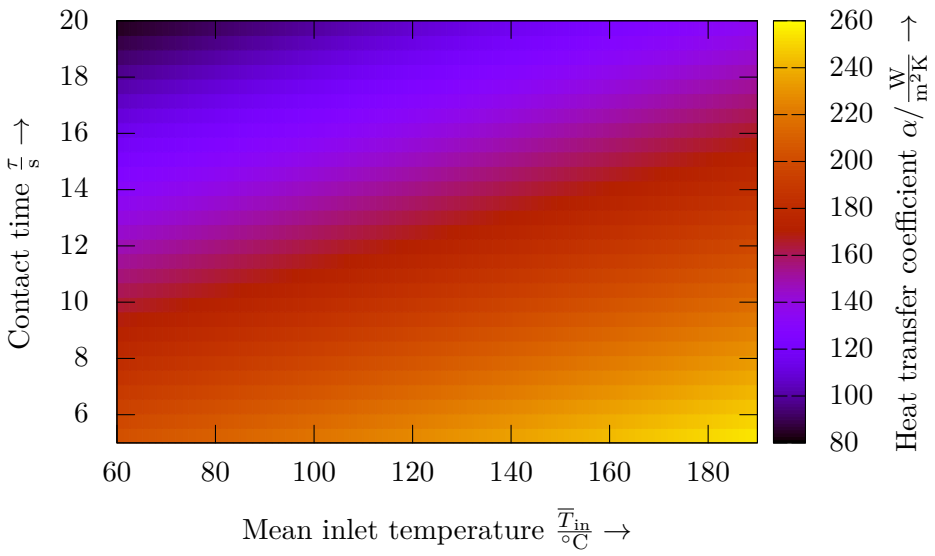

Figure 5.11: Fitted heat transfer coefficient for low temperatures

The polynomial obtained for the heat transfer coefficient model is rather simple,

$$\alpha = b_0 + b_1 \cdot \overline{T}_{\mathrm{in}} + b_2 \cdot \tau. \tag{5.28}$$

The adjusted coefficient of determination is fairly low for this regression. Its value is given in table 5.4 together with the regression coefficients.

Table 5.4: Regression coefficients and adjusted coefficients of determination for low temperature heat transfer measurements

Coefficient	Associated factor	Coefficient value
b_0	-	221.28
b_1	$\overline{T}_{\text{in}}$	0.3981
b_2	τ	−8.177
$\hat{R}^2$		0.6773

5.4 High Temperature Measurements

The possible number of experiments to be conducted per day is much lower for high temperature measurements due to long heating and cooling periods of the furnaces. Consequently, the high temperature measurement procedure differs from the one for the low temperature measurements. Together with the obtained results, it will be presented in this section.

5.4.1 Preheating

Heat losses to the test stand during the high temperature measurements are likely to be substantially higher than those during the low temperature measurements. It was therefore contemplated to preheat the test stand in order to limit the temperature drops between the chambers.
In a first test hot air of $T \approx 600\,^{\circ}\text{C}$ was introduced into the top chambers with all feeders opened. Downstream the top chambers the temperature increased slowly. All chamber temperatures showed a quick decline after stopping the air flow. Despite thermal insulation, several minutes of hot air heating also caused the linear actuators to approach their maximum operating temperature.
In addition, a prior heating run with heated particles and spheres was examined. It illustrated in the same drawback as before: All chamber temperatures quickly declined to values below $100\,^{\circ}\text{C}$. It was regarded difficult to provide constant initial conditions for each run under these circumstances. All runs were thus performed with an initial test stand temperature close to ambient temperature.

5.4.2 Influencing Factors

Within the scope of this work, the heat transfer coefficient for high temperatures could not be investigated for the same extent of factors as in the low temperature measurements with respect to limited time. This procedure, however, is well-founded when looking at the low temperature results: The two remaining significant factors on the heat transfer coefficient were found to be the mean inlet temperature $\overline{T}_{\text{in}}$ and the contact time τ. These were chosen for investigation in the high temperature measurements and varied over two levels each, forming a full factorial test plan. Every factor combination was replicated three times in order to assess measurement uncertainty from unidentified effects.

Levels for the mean inlet temperature of $\overline{T}_{\mathrm{in}} = 950\,^{\circ}\mathrm{C}$ and $1050\,^{\circ}\mathrm{C}$ were chosen in combination with a temperature difference between spheres and particles of $\Delta T_{\mathrm{in}} = T_{\mathrm{S}} - T_{\mathrm{P}} = 100\,\mathrm{K}$. Particle temperatures exceeding $1000\,^{\circ}\mathrm{C}$ caused sintering inside the crucible leading to difficulties during experimentation. The contact time takes values of $\tau = 5\,\mathrm{s}$ and $13\,\mathrm{s}$. Table 5.5 summarizes the tested factor levels and chosen values for the other factors from section 5.3.1 that were held constant.

Table 5.5: Influencing factors and their levels for high temperature measurements

Factor	Symbol	Levels	Unit
Mean inlet temperature	$\overline{T}_{\mathrm{in}}$	950, 1050	°C
Contact time	τ	5, 13	s
Diameter of particles	d_{P}	0.97	mm
Diameter of heat transfer spheres	d_{S}	4.95	mm
Mass ratio	X_{m}	0.6	-
Inlet temperature difference	ΔT	100	K
Direction of heat transfer	-	$T_{\mathrm{P,in}} < T_{\mathrm{S,in}}$	-

5.4.3 Offset Measurements

Since the high temperature measurements encompass four different factor combinations, there was not a complete test campaign conducted for offset measurements in the relevant temperature range. The occurring deviations were instead measured for each combination individually. This was done in two different ways. In the first way, sphere and particle temperature drops were measured within the same run as in the low temperature offset measurements. Both species were heated to the mean of the temperatures used in the heat transfer experiment. As an example, if the heat transfer run comprises a particle temperature of $900\,^{\circ}\mathrm{C}$ and a sphere temperature of $1000\,^{\circ}\mathrm{C}$, an inlet temperature of $950\,^{\circ}\mathrm{C}$ for both species was chosen for the corresponding offset measurement run. This way is referred to as *combined measurement*.

In the second way, particle and sphere temperature drops were measured separately. Each species was measured individually with the other chamber remaining void. For this purpose they were heated to the respective temperatures they take in the heat transfer measurements. Thus, for the example given above, instead of one combined offset run at $950\,^{\circ}\mathrm{C}$, two runs – one for particles at $900\,^{\circ}\mathrm{C}$ and one for spheres at $1000\,^{\circ}\mathrm{C}$ – were conducted. Below, this way is referred to as *individual measurement*. All offset measurements were further replicated once (two runs total). This is done in order to test the repeatability of both ways and obtain better estimates for the temperature drops.

5.4.4 Results

Offset Measurements

Table 5.6 gives a résumé of the temperature drops evaluated from the two different offset measurement ways. The given values are average values calculated from the results of two runs each. The values in parentheses are the deviations between the respective two particular values.

Table 5.6: Average temperature drops measured in two ways for high temperature measurements (deviations between individual values in parentheses)

	Combined measurement		Individual measurement	
Quantity	$\overline{T}_{\mathrm{in}} = 950\,^{\circ}\mathrm{C}$	$\overline{T}_{\mathrm{in}} = 1050\,^{\circ}\mathrm{C}$	$\overline{T}_{\mathrm{in}} = 950\,^{\circ}\mathrm{C}$	$\overline{T}_{\mathrm{in}} = 1050\,^{\circ}\mathrm{C}$
ΔT_{TL}	−53.7 (4.6)	−73.5 (17.5)	−40.4 (5.0)	−38.7 (4.3)
ΔT_{TR}	−64.3 (3.5)	−71.1 (5.0)	−80.4 (5.8)	−94.3 (5.4)
ΔT_{EL}	21.1 (8.3)	33.1 (7.2)	48.6 (4.9)	34.3 (15.6)[1]
ΔT_{ER}	24.5 (14.6)	22.5 (3.9)	39.3 (4.7)	46.5 (0.9)

There is a major difference between values obtained from different ways of measurement. The temperature drops from the top chambers to the heat transfer chambers are similar for combined measurement, but differ drastically for individual measurement. Significantly higher values for ΔT_{TR} are measured in the latter case, whereas those for ΔT_{TL} are significantly lower. This points to a considerable difference of heat losses of particles and spheres above the heat transfer chamber. The results from the individual measurements are plausible since the total surface area of the particles exceeds that of the spheres by a factor of approximately five. It is thus to be supposed that by combined measurement of particle and sphere temperatures the evaluated heat transfer chamber inlet temperatures are biased. The combined measurement delivers lower temperature drops below the heat transfer chamber, which may be caused by the higher absolute heat capacity introduced into the test stand. The temperature drops are not clearly increasing with the mean temperature, which may be due to high variability between the particular runs and a low number of replications. For the assumption of improved prediction and a lower mean difference between the particular values, the results from the individual measurements are used for correction of the heat transfer measurement results.

Heat Transfer Measurements

The values for the heat transfer coefficient α calculated from the high temperature measurement results are depicted in figure 5.12. All four factor combinations were measured three times each.

The results show a comprehensible general development similar to the low temperature measurement: The heat transfer coefficient rises with increasing mean inlet temperatures and declining contact times. Indeed, a considerable irregularity is apparent – the values for $\overline{T}_{\mathrm{in}} = 950\,^{\circ}\mathrm{C}$

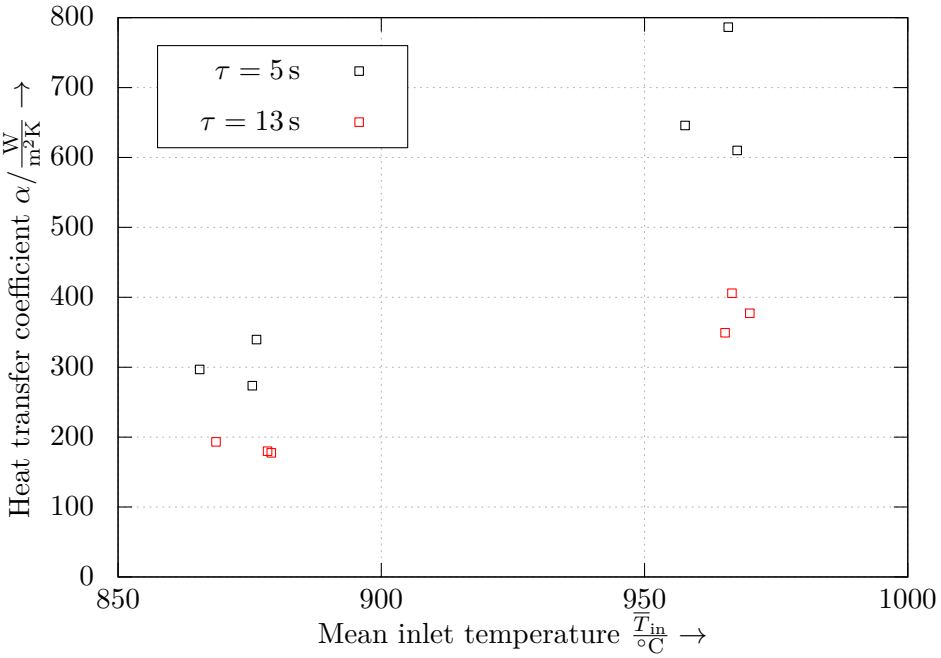

Figure 5.12: Heat transfer coefficient for high temperature measurements

are lower than the maximum values obtained from the low temperature measurements. This indicates systematic biases possibly introduced by the offset measurements.

The influence of the measured temperature drops on the values of the heat transfer coefficient are significant. The reading point with the maximum value for α of approximately 786 $\frac{\mathrm{W}}{\mathrm{m^2K}}$ results in a value of $\alpha = 418\,\frac{\mathrm{W}}{\mathrm{m^2K}}$ when correcting it by the offset results from the combined measurement.

The standard deviations for each factor combination are stated in table 5.7 together with the particular numerical values of α. A discussion of the standard deviations regarding the results of the uncertainty analysis from the subsequent section are subject to section 5.6.

Table 5.7: Heat transfer coefficients and their standard deviations for high temperature measurements (in $\frac{\mathrm{W}}{\mathrm{m^2K}}$)

$\overline{T}_{\mathrm{in}}/^\circ\mathrm{C}$	$\tau = 5\,\mathrm{s}$				$\tau = 13\,\mathrm{s}$			
	Run 1	Run 2	Run 3	std.dev.	Run 1	Run 2	Run 3	std.dev.
950	273.6	296.8	339.5	33.4	193.2	179.9	177.5	8.5
1050	645.8	610.1	786.4	93.2	405.8	377.2	349.3	28.2

5.5 Analysis of Measurement Uncertainty

The high number of runs conducted for the low temperature measurements provide a good statistical basis for the estimation of the regression coefficient and the prediction of heat transfer coefficients. As the low temperature measurements were primarily dedicated to

identify the most significant factors, an uncertainty analysis is second-tier for this case. The detailed investigation of uncertainty contributions and their extents is though crucial with respect to the high temperature measurements. The respective results are of importance for a quantitative evaluation of the investigated heat recovery concept. In addition, the different uncertainty contributions are likely to be increased for high temperatures. The analysis of measurement uncertainty covered in this section was therefore conducted for the high temperature measurements.

5.5.1 Uncertainties Assigned to Input Quantities

In this section the uncertainties assigned to the different input quantities of the equation for the heat transfer coefficient (5.11) are determined. As will be shown in more detail below, the uncertainty extents depend on the respective input quantities' values via the sensitivity coefficients. As the present uncertainty analysis is related to the high temperature measurements, these are given by the corresponding factor levels stated in table 5.5. Accordingly, the sphere diameter d_S, the particle mass m_P and sphere mass m_S remain constant, whereas the uncertainties are calculated for varying contact times, temperatures and dependent material properties. Numeric results are to be found in section 5.5.2.

Temperatures of Particles $T_{\mathrm{P,in}}/T_{\mathrm{P,out}}$ and Spheres $T_{\mathrm{S,in}}/T_{\mathrm{S,out}}$ The uncertainties in temperature results obtained from thermocouple measurements are stated in the calibration certificate of the temperature block calibrator. The uncertainty in each thermocouple first contributes to the average chamber temperature. The uncertainty of averaged temperature values can be given as a function of the number of individual values. With the averaged value

$$\overline{T} = \frac{1}{n}\sum_{i=1}^{n} T_i, \tag{5.29}$$

the uncertainty of the averaged value becomes according to equation 2.13:

$$u(\overline{T}) = \sqrt{\sum_{i=1}^{n}\left(\frac{\partial \overline{T}}{\partial T_i}\right)^2 u^2(T_i)} = \sqrt{\sum_{i=1}^{n}\left(\frac{1}{n}\right)^2 u^2(T_i)} \tag{5.30}$$

As all thermocouples are of the same type and were calibrated in the same device, they all hold the same uncertainty. This justifies the simplification of $u(T_1) = u(T_2) = ... = u(T)$. Equation 5.30 then turns to

$$u(\overline{T}) = \sqrt{\sum_{i=1}^{n}\left(\frac{1}{n}\right)^2 u^2(T)} = \sqrt{n \cdot \left(\frac{1}{n}\right)^2 u^2(T)} = \frac{u(T)}{\sqrt{n}}. \tag{5.31}$$

According to equations 5.15 to 5.18, the temperature values used for the calculation of the heat transfer coefficient (equation 5.11) depend on the temperatures measured in the top and end chambers and the correction values, *i. e.* the temperature drops determined by the offset measurements. The uncertainties of the latter will be evaluated first.

Since a mass ratio of $X_\mathrm{m} = 0.6$ was applied for the high temperature measurements, the top and end chamber temperatures were averaged over values obtained from two thermocouples

each. For the individual offset measurements, one thermocouple was used to measure the heat transfer chamber inlet temperature and four thermocouples were used for the heat transfer chamber outlet temperature. The uncertainties assigned to these correction values are

$$u(\Delta T_{\mathrm{TL}}) = u(\Delta T_{\mathrm{TR}}) = \sqrt{u^2(T) + \left(\frac{u(T)}{\sqrt{2}}\right)^2} = \sqrt{\frac{3}{2}}\, u(T) \tag{5.32}$$

and

$$u(\Delta T_{\mathrm{EL}}) = u(\Delta T_{\mathrm{ER}}) = \sqrt{\left(\frac{u(T)}{\sqrt{4}}\right)^2 + \left(\frac{u(T)}{\sqrt{2}}\right)^2} = \frac{\sqrt{3}}{2}\, u(T). \tag{5.33}$$

The uncertainties in the corrected temperatures result from the measurement of the uncorrected temperature and the uncertainties in the correction values as specified above. A difference arises between the uncertainties in the heat transfer chamber inlet temperatures and those in the outlet temperatures:

$$u(T_{\mathrm{S,in}}) = u(T_{\mathrm{P,in}}) = \sqrt{\left(\sqrt{\frac{1}{2}}\, u(T)\right)^2 + \left(\sqrt{\frac{3}{2}}\, u(T)\right)^2} = \sqrt{2} u(T) \tag{5.34}$$

$$u(T_{\mathrm{S,out}}) = u(T_{\mathrm{P,out}}) = \sqrt{\left(\sqrt{\frac{1}{2}}\, u(T)\right)^2 + \left(\frac{\sqrt{3}}{2}\, u(T)\right)^2} = \frac{\sqrt{5}}{2} u(T) \tag{5.35}$$

The numeric values for $u(T)$ depend on the measured temperature; according to the calibration certificate of the calibrator it is $u(T) = 1.25\,\mathrm{K}$ for $600\,^{\circ}\mathrm{C} \leq T < 900\,^{\circ}\mathrm{C}$ and $u(T) = 2.25\,\mathrm{K}$ for $900\,^{\circ}\mathrm{C} \leq T \leq 1200\,^{\circ}\mathrm{C}$.

Diameter of Spheres d_{S} The calculation of the corrected sphere diameter d_{S} according to equation 5.21 depends on three input quantities. These are the sphere diameter $d_{\mathrm{S},\infty}$ measured at ambient temperature, the coefficient of thermal expansion a_{L} and the mean sphere temperature $\overline{T}_{\mathrm{S}}$. All these quantities carry an uncertainty that will be outlined below.

The uncertainty in the sphere diameter $d_{\mathrm{S},\infty}$ at ambient temperature is due to uncertainties in the measurement system (*i. e.* the flat bed scanner), the size of and the variance within the sample of spheres selected for measurement.

An uncertainty contribution results from the discretization of the scanner's image sensor. The maximum deviation between the measured and the actual particle or sphere diameter is the width corresponding to two pixels. The samples was scanned with a resolution of 2400 dpi, one pixel thus spans a length of $\frac{1\,\mathrm{in}}{2400} = \frac{25.4\,\mathrm{mm}}{2400} = 0.0106\,\mathrm{mm}$. The distribution of possible diameters within this range is rectangular; the uncertainty contribution due to discretization is thus calculated in compliance with equation 2.9 using the half width of the interval,

$$u_{\mathrm{discr}}(d_{\mathrm{S},\infty}) = \frac{0.0106\,\mathrm{mm}}{\sqrt{3}} = 6.11 \cdot 10^{-3}\,\mathrm{mm}. \tag{5.36}$$

Other miscellaneous uncertainties in the scanner are very hard to determine in detail as there is no correspondent information available by a handbook or the like. An analysis of aberrations occurring in the optical system is beyond the scope of this work. For the present uncertainty analysis, it is assumed that the uncertainty arising from potential unknown effects in the

scanner is in the order of $u_{\mathrm{dis}}(d_{\mathrm{S}})$. It is estimated that they lead to a maximum deviation of a size corresponding to triple the size of the maximum possible deviation due to discretization, that is six pixels. In this case it is unphysical to suppose a rectangular distribution, because several effects are likely to be composed. The triangular distribution (equation 2.10) is thus applied:

$$u_{\mathrm{misc}}(d_{\mathrm{S},\infty}) = \frac{3 \cdot 0.0106\,\mathrm{mm}}{\sqrt{6}} = 0.0130\,\mathrm{mm}. \tag{5.37}$$

The significance of the diameter of the measured sample for that of the total population is characterized by the standard deviation of the mean. The sample consisted of 400 spheres, which means 400 observations were made with a standard deviation of the diameter of 0.14 mm (Felinks et al. 2015). Referred to equation 2.8 the uncertainty is given as the standard deviation divided by the number of observations,

$$u_{\mathrm{sample}}(d_{\mathrm{S},\infty}) = \frac{s(d_{\mathrm{S},\infty})}{\sqrt{n}} = \frac{0.14\,\mathrm{mm}}{\sqrt{400}} = 7 \cdot 10^{-3}\,\mathrm{mm}. \tag{5.38}$$

The resulting standard uncertainty in the sphere diameter at ambient temperature becomes

$$u(d_{\mathrm{S},\infty}) = \sqrt{u^2_{\mathrm{discr}}(d_{\mathrm{S},\infty}) + u^2_{\mathrm{misc}}(d_{\mathrm{S},\infty}) + u^2_{\mathrm{sample}}(d_{\mathrm{S},\infty})} = 0.016\,\mathrm{mm}. \tag{5.39}$$

In (Martienssen and Warlimont 2005) the coefficient of linear thermal expansion is specified as $a_{\mathrm{L}} = 6...8 \cdot 10^{-6}\,\frac{1}{\mathrm{K}}$. The median value was chosen for equation 5.21; the lack of knowledge about the actual value of a_{L} is regarded as an uncertainty contribution with rectangular distribution,

$$u(a_{\mathrm{L}}) = \frac{1 \cdot 10^{-6}\,\frac{1}{\mathrm{K}}}{\sqrt{3}} = 0.577 \cdot 10^{-6}\,\frac{1}{\mathrm{K}}. \tag{5.40}$$

The uncertainty in the measured temperature is explicated in the respective paragraph. With the equation for the average sphere temperature (equation 5.20), its uncertainty is determined by

$$u(\overline{T}_{\mathrm{S}}) = \sqrt{\frac{u^2(T_{\mathrm{S,in}})}{4} + \frac{u^2(T_{\mathrm{S,out}})}{4}} = \sqrt{\frac{\left(\sqrt{2}\,u(T)\right)^2}{4} + \frac{\left(\frac{\sqrt{5}}{2}\,u(T)\right)^2}{4}} = \frac{\sqrt{13}}{4}\,u(T). \tag{5.41}$$

The uncertainties in the inlet and outlet temperatures of spheres in the heat transfer chamber are the same as the uncertainty due to thermocouple measurement are equal for each thermocouple.

The combined uncertainty in the corrected sphere diameter d_{S} finally results in

$$\begin{aligned} u(d_{\mathrm{S}}) &= \sqrt{\left(\frac{\partial d_{\mathrm{S}}}{\partial d_{\mathrm{S},\infty}}\right)^2 u^2(d_{\mathrm{S},\infty}) + \left(\frac{\partial d_{\mathrm{S}}}{\partial a_{\mathrm{L}}}\right)^2 u^2(a_{\mathrm{L}}) + \left(\frac{\partial d_{\mathrm{S}}}{\partial \overline{T}_{\mathrm{S}}}\right)^2 u^2(\overline{T}_{\mathrm{S}})} \\ &= \sqrt{\left(1 + a_{\mathrm{L}}\overline{T}_{\mathrm{S}}\right)^2 u^2(d_{\mathrm{S},\infty}) + \left(d_{\mathrm{S},\infty}\overline{T}_{\mathrm{S}}\right)^2 u^2(a_{\mathrm{L}}) + (d_{\mathrm{S},\infty}a_{\mathrm{L}})^2\, u^2(\overline{T}_{\mathrm{S}})} \end{aligned} \tag{5.42}$$

and has to be evaluated depending on the temperature.

Density of Spheres ρ_S The temperature dependent density is calculated from the measured sphere density at ambient temperature $\rho_{S,\infty}$, the coefficient of linear thermal expansion a_L and the mean sphere temperature $\overline{T}_S$, see equation 5.22.

The sphere density $\rho_{S,\infty}$ at ambient temperature was measured with a pycnometer. Uncertainties in the pycnometer volume are most presumably to be neglected. Other uncertainties might arise from reading, density differences in the measured samples or weighing of the displaced water. Three independent measurements were conducted, so their best estimate is obtained by calculating the standard deviation of the mean,

$$u(\rho_{S,\infty}) = \frac{s(\rho_{S,\infty})}{\sqrt{3}} = 1.71\,\frac{\mathrm{kg}}{\mathrm{m}^3}. \tag{5.43}$$

The uncertainties in the coefficient of thermal expansion $u(a_L)$ and the one in the sphere temperature $u(\overline{T}_S)$ are already known from the previous paragraph.

The combined uncertainty in the corrected density thus becomes

$$\begin{aligned} u(\rho_S) &= \sqrt{\left(\frac{\partial \rho_S}{\partial \rho_{S,\infty}}\right)^2 u^2(\rho_{S,\infty}) + \left(\frac{\partial \rho_S}{\partial a_L}\right)^2 u^2(a_L) + \left(\frac{\partial \rho_S}{\partial \overline{T}_S}\right)^2 u^2(\overline{T}_S)} \\ &= \sqrt{\left(\frac{1}{1+3a_L\overline{T}_S}\right)^2 u^2(\rho_{S,\infty}) + \left(\frac{3\rho_{S,\infty}\overline{T}_S}{(1+3a_L\overline{T}_S)^2}\right)^2 u^2(a_L) + \left(\frac{3\rho_{S,\infty}a_L}{(1+3a_L\overline{T}_S)^2}\right)^2 u^2(\overline{T}_S)} \end{aligned} \tag{5.44}$$

Specific Heat Capacity of Particles $c_{p,P}$ and Spheres $c_{p,S}$ No information is given on the measurement uncertainties assigned to the tabulated molar heat capacity values in (Barin 1995). They are estimated not exceed the decimal precision of 0.002 % of the given values about more than one order of magnitude and are hence to be neglected. A considerable uncertainty contribution by potential interpolation errors is further not expected as the differences in molar heat capacities between the given values are low compared to absolute values and the fitting functions are of good quality. Relevant uncertainties in the specific heat capacities may arise from the uncertainty in the particle or sphere temperature used for calculation in the fitting polynomials. As some polynomials for the respective components are discontinuous, the uncertainties are estimated for the main components – ZrO_2 for particles and Al_2O_3 for spheres.

The maximum temperature standard uncertainty for the temperature range between $T = 900\,^\circ\mathrm{C}$ and $T = 1200\,^\circ\mathrm{C}$ is $u_{\max}(T) = 2.25\,\mathrm{K}$. With the maximum temperature reached in the high temperature measurements of $T_{\max} = 1300\,\mathrm{K}$ the maximum standard uncertainty in the molar heat capacity of ZrO_2 becomes

$$u_{\max}(C_{m,ZrO_2}) = \sqrt{\left(\left.\frac{\partial C_{m,ZrO_2}}{\partial T}\right|_{T=T_{\max}}\right)^2 u^2_{\max}(T)} = 0.040\,\frac{\mathrm{J}}{\mathrm{mol\,K}} \tag{5.45}$$

For the spheres is found analogously:

$$u_{\max}(C_{m,Al_2O_3}) = \sqrt{\left(\left.\frac{\partial C_{m,Al_2O_3}}{\partial T}\right|_{T=T_{\max}}\right)^2 u^2_{\max}(T)} = 0.077\,\frac{\mathrm{J}}{\mathrm{mol\,K}} \tag{5.46}$$

The fitting functions for the individual components are found in annex A.

It can be assumed that the uncertainties in the molar heat capacities of the other components are of the same order since they are calculated by similar fitting functions. The specific heat capacities for particles and spheres are calculated according to 5.26 and their uncertainties are

$$u(c_{\mathrm{p,P}}) = \frac{u(C_{\mathrm{m,P}})}{M_{\mathrm{P}}} = 0.31\,\frac{\mathrm{J}}{\mathrm{kgK}} \tag{5.47}$$

and

$$u(c_{\mathrm{p,S}}) = \frac{u(C_{\mathrm{m,S}})}{M_{\mathrm{S}}} = 0.82\,\frac{\mathrm{J}}{\mathrm{kgK}}, \tag{5.48}$$

respectively.

Contact Time τ A variability in the durations of filling the heat transfer chamber was observed during the mixture optimization tests. These are in the range of $\tau_{\mathrm{fill}} = 3.5 \pm 0.3\,\mathrm{s}$. Low deviations are more likely to appear, thus the triangular distribution is applied, leading to a standard uncertainty in the contact time τ due to varying filling times of

$$u_{\mathrm{fill}}(\tau) = \frac{0.3\,\mathrm{s}}{\sqrt{6}} = 0.12\,\mathrm{s}. \tag{5.49}$$

The variation of the filling time can only be evaluated for mixtures at ambient temperature. An additional uncertainty accounting for deviations occurring at high temperatures is thus estimated:

$$u_{\mathrm{temp}}(\tau) = \frac{0.2\,\mathrm{s}}{\sqrt{6}} = 0.08\,\mathrm{s}. \tag{5.50}$$

The combined uncertainty adds up to

$$u(\tau) = \sqrt{u_{\mathrm{fill}}^2(\tau) + u_{\mathrm{temp}}^2(\tau)} = 0.15\,\mathrm{s}. \tag{5.51}$$

Mass of Particles m_{P} Spheres m_{S} Sources of uncertainties in the sphere and particle masses are the weighing accuracy and possible losses during the measurement process. The latter may be caused by sticking to the crucibles (especially at high temperatures), spillage when filling the top chambers and jamming between chambers and feeders.

The masses of particles and spheres directly affect the calculated transferred amounts of heat. In this context a considerable influence of the respective masses inside the heat transfer chamber during contact time on the heat transfer coefficient's uncertainty is expected. The effect of varying masses on the temperatures measured in the chambers is assumed to be negligible. The distance between the topmost immersed thermocouple and the filling level amounts to 2.5 cm, compare figure 4.5. The upper estimate of mass losses due to sticking and jamming of 10 g corresponds to a level decrease of approximately 2 mm. This change is not assumed to have an considerable effect on the measured temperature.

Uncertainties arising from balance inaccuracy are in the order of milligrams and thus negligible compared to the mass losses of several grams during the experiment. The finite weight of a single sphere of up to 0.3 g causes a maximum deviation of the actual mass from the nominal mass of 0.15 g. For particles this value was estimated as 0.05 g, although the mass of a single particle is much lower. The corresponding uncertainties are calculated for a rectangular distribution,

$$u_{\text{weigh}}(m_{\text{S}}) = \frac{0.15\,\text{g}}{\sqrt{3}} = 0.087\,\text{g} \tag{5.52}$$

$$u_{\text{weigh}}(m_{\text{P}}) = \frac{0.05\,\text{g}}{\sqrt{3}} = 0.029\,\text{g} \tag{5.53}$$

The amounts of sticking, spilled and jammed particles and spheres were identified experimentally. As briefly mentioned above, maximum total mass losses of 10 g for spheres and 2 g for particles were observed, combined for all types of losses. In this case an asymmetric distribution is applied, compare equation 2.11. The related standard uncertainties become

$$u_{\text{loss}}(m_{\text{S}}) = \frac{10\,\text{g}}{\sqrt{12}} = 2.89\,\text{g} \tag{5.54}$$

$$u_{\text{loss}}(m_{\text{P}}) = \frac{2\,\text{g}}{\sqrt{12}} = 0.577\,\text{g} \tag{5.55}$$

It becomes apparent that uncertainties due to weighing are much lower than those due to losses during experimentation and are actually negligible. The combined uncertainties are thus equal to the latter ones, $u(m_{\text{S}}) = u_{\text{loss}}(m_{\text{S}})$ and $u(m_{\text{P}}) = u_{\text{loss}}(m_{\text{P}})$.

5.5.2 Uncertainty Results

The uncertainties assigned to the values for the heat transfer coefficient calculated by equation 5.11 are obtained by applying the law of propagation of uncertainty (equation 2.13). It was mentioned above that the sensitivity coefficients depend on the respective values of the input quantities and are not constant. This causes varying uncertainty values among the runs with nominally the same conditions. The sensitivity coefficients' equations are given in annex B. The standard uncertainties assigned to the heat transfer coefficient results from high temperature measurements are given in table 5.8 for each individual run.

Table 5.8: Standard uncertainties $u(\alpha)$ in heat transfer coefficients and their means for high temperature measurements (in $\frac{\text{W}}{\text{m}^2\text{K}}$)

$\overline{T}_{\text{in}}$/°C	$\tau = 5\,\text{s}$				$\tau = 13\,\text{s}$			
	Run 1	Run 2	Run 3	mean	Run 1	Run 2	Run 3	mean
950	23.0	22.8	28.4	24.7	14.7	15.1	15.9	15.2
1050	57.9	61.9	103.6	74.5	79.9	64.1	56.6	66.9

The substantially higher standard uncertainties for high nominal temperatures are primarily caused by high thermocouple uncertainties for real temperatures above 900 °C. There is a decrease of the uncertainties for higher contact times due to the decreasing relative uncertainty in contact time $\frac{u(\tau)}{\tau}$. The values are substantial with respect to the absolute values for α; the relative uncertainties range between 7 % and 20 %.

The individual uncertainty contributions can be evaluated by calculating their weighting factors according to equation 2.14. These are given in table 5.9 for all uncertainty components, averaged over three runs for each factor combination.

Table 5.9: Weightings of uncertainty contributions in heat transfer coefficients for high temperature measurements (in %, rounded to one decimal place)

Component	$\overline{T}_{\mathrm{in}} = 950\,^{\circ}\mathrm{C}$ $\tau = 5\,\mathrm{s}$	$\overline{T}_{\mathrm{in}} = 950\,^{\circ}\mathrm{C}$ $\tau = 13\,\mathrm{s}$	$\overline{T}_{\mathrm{in}} = 1050\,^{\circ}\mathrm{C}$ $\tau = 5\,\mathrm{s}$	$\overline{T}_{\mathrm{in}} = 1050\,^{\circ}\mathrm{C}$ $\tau = 13\,\mathrm{s}$
$u(T_{\mathrm{P,in}})$	2.2	0.9	0.4	0.1
$u(T_{\mathrm{S,in}})$	17.5	9.0	2.3	0.5
$u(T_{\mathrm{P,out}})$	11.7	16.9	40.2	47.0
$u(T_{\mathrm{S,out}})$	54.5	70.9	48.5	52.0
$u(m_{\mathrm{P}})$	0.0	0.0	0.0	0.0
$u(m_{\mathrm{S}})$	0.2	0.2	0.0	0.0
$u(c_{\mathrm{p,P}})$	0.0	0.0	0.0	0.0
$u(c_{\mathrm{p,S}})$	0.0	0.0	0.0	0.0
$u(d_{\mathrm{S}})$	0.2	0.2	0.1	0.0
$u(\rho_{\mathrm{S}})$	0.1	0.1	0.0	0.0
$u(\tau)$	13.6	1.9	8.4	0.4

Uncertainties in the masses and specific heat capacities of particles and spheres as well as in the spheres' diameter and density hold a negligible influence on the combined standard uncertainty. The most significant contributions are found to be the outlet temperatures of particles $u(T_{\mathrm{P,out}})$ and spheres $u(T_{\mathrm{S,out}})$ due to high values of the respective sensitivity coefficients. This becomes clear when considering the temperature development of particles and spheres: As the outlet temperature difference is much lower than the inlet temperature difference, uncertainties in the measured outlet temperatures have a stronger impact on the mean logarithmic temperature. This effect is further emphasized for high contact times resulting in lower outlet temperature differences. However, thus rising uncertainties are partly compensated by decreasing relative uncertainties in the contact time. The high weightings for the sphere temperature uncertainties for $\overline{T}_{\mathrm{in}} = 950\,^{\circ}\mathrm{C}$ is explained by higher thermocouple uncertainties above 900 °C according to the calibration certificate.

5.6 Review and Discussion

The low temperature investigation of the different factors with expected relevant influence on the heat transfer coefficient revealed the contact time τ and the mean inlet temperature $\overline{T}_{\mathrm{in}}$ to be of major importance. These findings had been anticipated: The contact time's effect results from the time-averaged calculation of the measured heat transfer coefficient (see section 5.1). In connection with declining temperature difference and heat flux over time, α and τ show an opposing trend. Despite the absence of substantial thermal radiation in the temperature range of 20...250 °C the mean inlet temperature considerably affects the heat transfer.

An improved heat transfer for smaller sphere and particle diameters could not be proven, even though it is predicted by the model of (Schlünder 1984). The mass ratio showed an ambiguous behavior that could not be plausibly interpreted by statistical means, also with respect to the

high spread of data points. This is not physically allegeable, because high mass fractions of particles or spheres in the mixture most likely reduce the effective contact surface area between them.

Changing temperature differences (for constant mean temperatures) do not have a remarkable influence on the heat transfer coefficient. This is comprehensible, since thus higher transferred amounts of heat are compensated by the rising logarithmic mean temperature in the denominator of equation 5.11. For the low temperature measurements the material properties' temperature dependency is negligible, whereas it could be of importance for temperatures around 1000 °C. Temperature dependent emissivities could necessitate to include the inlet temperature difference as a factor in potential measurement campaigns for high temperatures. The same applies for the direction of heat transfer – it is insignificant for the low temperature results, but makes a difference when thermal radiation becomes relevant.

The high temperature measurements clearly reveal the increased temperature influence on the heat transfer coefficient. For constant contact times the average values from three runs are approximately doubled for the higher temperature level. Still the contact time remains an important factor. Doubts about the absolute values of heat transfer coefficients however remain. For a contact time of 13 s and an effective mean inlet temperature of about 875 °C the obtained average heat transfer coefficient is $\alpha = 184\,\frac{\mathrm{W}}{\mathrm{m^2K}}$. This value is lower than that for the same contact time and a mean inlet temperature of 190 °C measured in the low temperature measurements. The validity of the remaining high temperature measurement results thus have to be questioned as well. The deviation is most probably due to the method of how the sphere and particle temperatures were corrected with respect to heat losses in the test stand.

The outcomes of replication tests for the combined offset measurement disclosed a relevant falsification of the measured temperature drops at high temperatures. The simultaneous measurement of particle and sphere temperatures within their mixture in the heat transfer chamber does not appear to be a valid procedure. Differences in the effective top chamber inlet temperatures of particles and spheres occur. This is presumably caused by variations in heating temperature due to different chamber furnaces, heating times and positions in the furnaces. Other than for the low temperature measurements there may further be substantial differences in heat losses from the top chambers to the heat transfer between particles and spheres.

Correcting the top and end chamber temperatures with the temperature drops obtained from the individual measurements could indeed correct the heat transfer coefficient values to a certain extent. Nevertheless, as mentioned above, the heat transfer results remain doubtful. The individual offset measurement method ignores the interaction between the two species' mass flows when filling the heat transfer chamber. It is to be assumed that the temperature drops are overestimated when measured individually. This could in fact lead to underestimated heat transfer coefficients: Temperature drops for particles and spheres both determined to be higher than real lead to lower values of transferred heat from the species of higher temperature.

Further departure from the actual prevailing temperatures could be induced by differing heat transfer chamber residence times of the mixture during an offset measurement run. The duration of temperature assimilation of the thermocouples in the heat transfer chamber amounts to a multiple of the contact times during heat transfer measurements. Moreover, the assimilation times vary between the offset measurement runs. This is a source of deviations for

the temperature drops from the heat transfer chamber to the end chambers. These directly affect the corrected heat transfer chamber outlet temperatures $T_{\mathrm{P,out}}$ and $T_{\mathrm{S,out}}$. Since these input variables to the heat transfer coefficient's equation hold the highest sensitivity coefficients (also compare table 5.9), a potential corresponding deviation has to be assumed.

A substantial spread of the individual results for α for each factor combination can be observed, see figure 5.12. The standard deviations related to the mean absolute values range between 5 % and 14 %. However, when calculating the standard uncertainties of the mean values obtained from three runs each (according to equation 2.8), these values are in the same range with the results of the uncertainty analysis, table 5.10.

Table 5.10: Comparison of uncertainties in the heat transfer coefficient, obtained from experiment and uncertainty analysis

	$\overline{T}_{\mathrm{in}} = 950\,^{\circ}\mathrm{C}$ $\tau = 5\,\mathrm{s}$	$\overline{T}_{\mathrm{in}} = 950\,^{\circ}\mathrm{C}$ $\tau = 13\,\mathrm{s}$	$\overline{T}_{\mathrm{in}} = 1050\,^{\circ}\mathrm{C}$ $\tau = 5\,\mathrm{s}$	$\overline{T}_{\mathrm{in}} = 1050\,^{\circ}\mathrm{C}$ $\tau = 13\,\mathrm{s}$
$u_{\mathrm{exp}}(\alpha)$	19.3	4.9	53.8	16.3
$u_{\mathrm{an}}(\alpha)$	24.7	15.2	74.5	66.9

The variability of the individual high temperature results is overestimated by the uncertainty analysis for all factor combinations. It can be deduced that other potential uncertainties are within certain limits and only moderately affect the measured heat transfer coefficient. These could arise from variabilities in mixture quality, thermal contact between thermocouple and bed, ambient temperature or in changes in the test stand, e. g. due to wear. However, the findings above concerning systematic effects, primarily on the measured temperature drops during offset measurements have to be regarded. Due to high uncertainty weightings for the heat transfer chamber outlet temperatures, special attention should be payed to a thorough measurement and correction of these values.

6 Genuine Countercurrent Heat Exchanger for Particles in Direct Contact

The heat recovery concept using quasi-countercurrent heat exchanger that was explicated in chapter 3 incorporates an inherent limitation of effectiveness. The maximum theoretical heat recovery rate can be derived analytically when assuming constant heat capacities for particles and spheres and a contact time in each stage going to infinity. For the optimal ratio of heat capacity rates of $\frac{\dot{C}_S}{\dot{C}_P} = 1$ and a number of stages n the heat recovery rate then becomes $\psi = \frac{1}{1+\frac{2}{n}}$. There is consequently a trade-off between the heat recovery rate and the cost for conveyance facilities connecting the stages. There is no such limit of theoretical effectiveness when applying countercurrent heat exchangers. Moreover, a countercurrent operation would considerably simplify the apparatus. In this chapter, a concept is proposed that allows to pass two species of solid particles in opposed direction in direct contact. It can be adapted to a heat recovery system using a particulate heat transfer medium as the regenerator.

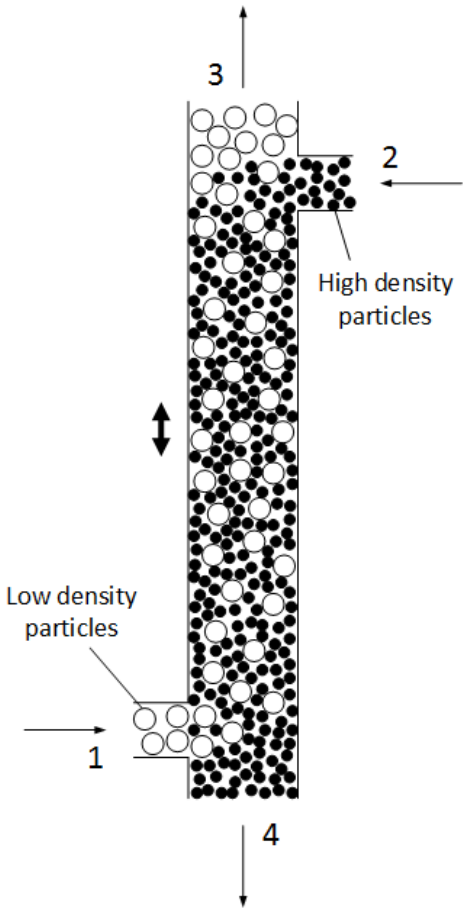

Figure 6.1: Particle flow in exemplary vertical container exposed to vibration

The heat exchanger makes use of the relative movement of particles of different bulk densities in agitated beds, as illustrated in figure 6.1. Exposing a corresponding mixture of different

particle species to vibration will make the high density particles descend, while those of lower density are forced upwards by buoyancy effects. Introducing the high density species at the top (2) of a vertical container and the low density species at the bottom (1) thus enables a countercurrent flow of particles in direct contact (Richter and Felinks 2015).

The basic working principle was demonstrated in a first test. For this, the zirconia-ceria particles of $d_P = 0.73\,\text{mm}$ and alumina spheres of $d_S = 4.95\,\text{mm}$ from the heat transfer measurements were used. A bed of particles was established upon a bed of spheres in a beaker connected to a vibrating plate. The arrangement of both species before and after an exposure to vibration for about 2 minutes is shown in figure 6.2.

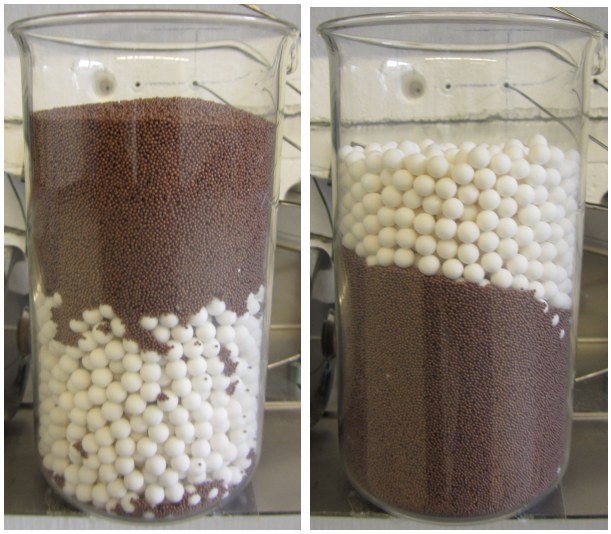

Figure 6.2: Arrangement of particles and spheres before (left) and after exposure to vibration

The vibration was generated by a vibration motor mounted to a metal sheet. Due to an asymmetric position of the beaker on the sheet relative to its fixation a three-dimensional oscillation is generated. The effect of directed oscillation in different dimensions on the flow and separation performance could be investigated for different particle density ratios and diameters.

Different ways of realizing the inlets and outlets of the container from figure 6.1 are conceivable. The high density particle outlet (4) could be equipped with a sieve or a rotating valve to control the high density particle flow rate. The low density particle outlet (3) could be realized as an open level drain with the high density particles entering through the same opening, for instance falling onto the bed of displaced low density particles. The force needed to introduce the low density particles at the bottom (1) could be raised by a conveyor auger. Alternatively, a column also exposed to vibration and connected to the inlet could lead to an effect similar to hydrostatic pressure difference, allowing to control the flow rate by the particle bed's level in the column.

Applying the presented heat exchanger concept to heat recovery from particles in thermochemical cycles allows to circumvent several drawbacks of the concepts presented in chapter 3. It avoids separating walls and high conveyance facilities, but allows a high contact surface area, relatively simple and scalable setup and high specific heat capacity of the regenerator.

7 Summary and Outlook

The present work was motivated by the analysis of a system for heat recovery from solid particles. It concerns the experimental investigation of heat transfer between the different species in a binary packed bed of zirconia-ceria particles and alumina spheres. An existing test stand was instrumented and put into operation for performing the experiments. It allows automated temperature measurement as well as mixing and separation of particles and spheres in batch operation. Modifications were applied to improve the homogeneity of the mixture in the corresponding heat transfer chamber.

Different factors were varied and tested on their influence on the heat transfer coefficient. These are the diameters of particles and spheres, the mean inlet temperature, the inlet temperature difference, the ratio of masses, the contact time and the direction of heat transfer.

A first experimental campaign was conducted in the temperature range between 20 °C and 250 °C in order to minimize temperature deviations due to heat losses in the test stand. Nevertheless, an individual offset measurement campaign was necessary to determine the temperature drops of particles and spheres between the measuring points and the heat transfer chamber. Its results were used to correct the temperature values taken during the actual heat transfer measurements. Both campaigns were planned with the help of Design of Experiments, allowing to obtain the desired information from a limited number of test runs. The statistical analysis revealed that in the considered temperature range, the contact time and the mean inlet temperature difference of particles and spheres are of significant influence. The heat transfer coefficient increases with increasing mean inlet temperatures and decreasing contact times. Other investigated factors were found to be of unphysical or negligible effect compared to the variance of measurement points. Values for the heat transfer coefficient of up to 260 $\frac{\mathrm{W}}{\mathrm{m^2K}}$ were evaluated.

Measurements of the heat transfer coefficient relevant for the proposed application were conducted in the temperature range of 900 °C and 1100 °C. With the mean inlet temperature and the contact time those factors were chosen for investigation in this case that showed a significant effect in the low temperature measurements. It became apparent that the influence of the temperature level is strongly increased, while the contact time is still of important effect. The maximum measured values reach 786 $\frac{\mathrm{W}}{\mathrm{m^2K}}$. However, doubts about the high temperature results remain, because the lowest values are lower than the highest values obtained in the low temperature measurements. This is connected to the way in which the temperature drops of particles and spheres in the test stand were measured. There is no method that allows to determine the drops occurring in the heat transfer experiment unambiguously. Here, the temperature drops were measured individually, neglecting the mutual thermal influence of particles and spheres and leading to underestimated heat transfer coefficients.

A detailed uncertainty analysis was performed concerning the high temperature measurements that takes into account all the elemental uncertainties in the quantities contributing to the calculated result. Most relative uncertainties assigned to the heat transfer coefficients from the individual high temperature measurement runs amount to approximately 10 %. Those

corresponding to high temperatures and high contact times are below 20 %. The experimental uncertainties calculated from replicated measurement runs are considerably lower. This indicates that all relevant uncertainty contributions have been taken into account.

An alternative heat recovery concept was proposed that circumvents inherent limitations of effectiveness as well as technical effort connected to the original concept. It employs genuine countercurrent heat exchangers for particles in direct contact using their density difference while being exposed to vibration.

Prospective studies should address the issue of offset measurements. A potential path could consist in the separate determination of temperature drops before and after the heat transfer chamber. The use of thermocouples with smallest sheath diameters allow the reduction of measurement times and consequently transient heat losses.

A complete test campaign is recommended for both offset measurements and high temperature heat transfer measurements involving all factors considered in the low temperature measurements. Relevant main effects and interactions can be expected due to temperature dependent material properties.

Bibliography

[Achternbosch and Bräutigam 2000] Achternbosch, M. ; Bräutigam, K.-R.: *Herstellung von Zementklinker. Verfahrensbeschreibung und Analysen zum Einsatz von Sekundärbrennstoffen*, Forschungszentrum Karlsruhe, Scientific report, 2000.

[Agrafiotis et al. 2015] Agrafiotis, Christos ; Roeb, Martin ; Sattler, Christian: A review on solar thermal syngas production via redox pair-based water/carbon dioxide splitting thermochemical cycles. In: *Renewable and Sustainable Energy Reviews* 42 (2015), pp. 254–285.

[Barin 1995] Barin, Ihsan: *Thermochemical Data of Pure Substances*. Weinheim : VCH, 1995.

[Bernhard 2004] Bernhard, Frank: *Technische Temperaturmessung. Physikalische und meßtechnische Grundlagen, Sensoren und Meßverfahren, Meßfehler und Kalibrierung*. Berlin : Springer, 2004.

[Brendelberger et al. 2014] Brendelberger, Stefan ; Felinks, Jan ; Roeb, Martin ; Sattler, Christian: Solid Phase Heat Recovery and Multi Chamber Reduction for Redox Cycles. In: *Proceedings of the ASME 2014 8th International Conference on Energy Sustainability & 12th Fuel Cell Science, Engineering and Technology Conference, ESFuelCell2014, June 29-July 2, Boston, Massachusetts, USA*, American Society of Mechanical Engineers, 2014.

[Chikh et al. 2014] Chikh, Houria ; Si-Ahmed, Fariza ; Afir, Arezki ; Pialoux, André: In-situ X-ray Diffraction Study of Alumina -Al2O3 Thermal Behavior. In: *International Journal of Recent Development in Engineering and Technology* 3 (2014), No. 2, pp. 137–143.

[Diver et al. 2010] Diver, Richard B. ; Miller, James E. ; Siegel, Nathan P. ; Moss, Timothy A.: Testing of a CR5 Solar Thermochemical Heat Engine Prototype. In: *Proceedings of the ASME 2010 4th International Conference on Energy Sustainability, ES2010, May 17-22, 2010, Phoenix, Arizona, USA* (2010), pp. 1–8.

[Ermanoski et al. 2014] Ermanoski, Ivan ; Miller, J. E. ; Allendorf, M. D.: Efficiency maximization in solar-thermochemical fuel production: challenging the concept of isothermal water splitting. In: *Phys. Chem. Chem. Phys.* 16 (2014), pp. 8418–8427.

[Ermanoski et al. 2013] Ermanoski, Ivan ; Siegel, Nathan P. ; Stechel, Ellen B.: A New Reactor Concept for Efficient Solar-Thermochemical Fuel Production. In: *Journal of Solar Energy Engineering* 135 (2013), pp. 3100201–3100210.

[Felinks et al. 2014] Felinks, Jan ; Brendelberger, Stefan ; Roeb, Martin ; Sattler, Christian ; Pitz-Paal, Robert: Heat recovery concept for thermochemical processes using a solid heat transfer medium. In: *Applied Thermal Engineering* 73 (2014), pp. 1004–1011.

[Felinks et al. 2015] Felinks, Jan ; Richter, Sebastian ; Lachmann, Bruno ; Brendelberger, Stefan ; Roeb, Martin ; Sattler, Christian ; Pitz-Paal, Robert: Particle-particle heat transfer coefficient in a binary packed bed. (2015). – submitted April 22, 2015.

[Hogan et al. 2013] Hogan, R. E. ; Miller, J. E. ; James, D. L. ; Chen, K. S. ; Diver, R. B.: Modeling Chemical and Thermal States of Reactive Metal Oxides in a CR5 Solar Thermochemical Heat Engine. In: *Journal of Solar Energy Engineering* 135 (2013), pp. 03100401–03100411.

[ISO/BIPM 2010] International Standardization Organisation / Bureau International des Poids et Mesures: *Evaluation of Data – Guide to the expression of uncertainty in measurement. JCGM 100:2008, GUM 1995 with minor corrections.* 2010.

[Kleppmann 2013] Kleppmann, Wilhelm: *Versuchsplanung. Produkte und Prozesse optimieren.* München : Hanser, 2013.

[Lachmann 2014] Lachmann, Bruno: *Entwicklung eines Teststandes zur Ermittlung des Wärmübergangskoeffizienten in einer Partikelschüttung*, Fachhochschule Köln, Studienarbeit, 2014.

[Lange et al. 2014] Lange, Matthias ; Roeb, Martin ; Sattler, Christian ; Pitz-Paal, Robert: T-S diagram efficiency analysis of two-step thermochemical cycles for solar water splitting under various process conditions. In: *Energy* 67 (2014), pp. 298–308.

[Lapp et al. 2012] Lapp, Justin ; Davidson, Jane H. ; Lipiński, Wojciech: Efficiency of two-step solar thermochemical non-stoichiometric redox cycles with heat recovery. In: *Energy* 37 (2012), pp. 591–600.

[Lapp et al. 2013] Lapp, Justin ; Davidson, Jane H. ; Lipiński, Wojciech: Heat Transfer Analysis of a Solid-Solid Heat Recuperation System for Solar-Driven Nonstoichiometric Redox Cycles. In: *Journal of Solar Energy Engineering* 135 (2013), pp. 03100401–03100411.

[Martienssen and Warlimont 2005] Martienssen, Werner ; Warlimont, Hans (Eds.): *Springer Handbook of Condensed Matter and Materials Data.* Berlin : Springer, 2005.

[Meier and Sattler 2009] Meier, Anton ; Sattler, Christian: Solar Fuels from Concentrated Sunlight. IEA SolarPACES Implementing Agreement. 2009.

[Montgomery 2013] Montgomery, Douglas C.: *Design and Analysis of Eperiments.* Singapore : John Wiley & Sons, 2013.

[Polifke and Kopitz 2011] Polifke, Wolfgang ; Kopitz, Jan: *Wärmeübertragung. Grundlagen, analytische und numerische Methoden.* München : Pearson Studium, 2011.

[Ratcliffe and Ratcliffe 2015] Ratcliffe, Colin ; Ratcliffe, Bridget: *Doubt-Free Uncertainty In Measurement.* Cham : Springer, 2015.

[Richter and Felinks 2015] Richter, Sebastian ; Felinks, Jan: *Direktkontakt Partikel-Partikel Vibrations-Wärmeübertrager/Reaktor im Gegenstrom.* 2015. – Internal invention announcement made demands on by the German Aerospace Center (DLR).

[Romero and Steinfeld 2012] Romero, Manuel ; Steinfeld, Aldo: Concentrating solar thermal power and thermochemical fuels. In: *Energy Environ. Sci.* 5 (2012), pp. 9234–9245.

[Schlünder 1984] Schlünder, Ernst-Ulrich: Heat transfer to packed and stirred beds from the surface of immersed bodies. In: *Chemical Engineering and Processing: Process Intensification* 18 (1984), No. 1, pp. 31–53.

[Siebertz et al. 2010] Siebertz, Karl ; van Bebber, David ; Hochkirchen, Thomas: *Statistische Versuchsplanung. Design of Experiments.* Heidelberg : Springer, 2010.

[Simonton and Stone 1986] Simonton, Ward ; Stone, Marvin: Counterflow Particle-To-Particle Heat Exchange. Part II. Design and Performance of a Prototype. In: *Transactions of the American Society of Agricultural Engineers* 29 (1986), No. 3, pp. 874–880.

[Steinfeld 2002] Steinfeld, Aldo: Solar hydrogen production via a two-step water-splitting thermochemical cycle based on Zn/ZnO redox reactions. In: *International Journal of Hydrogen Energy* 27 (2002), pp. 611–619.

[VDI 2013] Verein Deutscher Ingenieure, VDI-Gesellschaft Verfahrenstechnik und Chemieingenieurwesen (Ed.): *VDI Wärmeatlas.* Berlin : Springer, 2013.

[Welford and Winston 1989] Welford, W. T. ; Winston, R.: *High Collection Nonimaging Optics.* San Diego : Academic Press, 1989.

A Molar Heat Capacity Fitting Functions

The fitting polynomials used to calculate the molar heat capacities of the chemical components of particles and spheres are given below. They are valid for $298\,\mathrm{K} \leq T \leq 1250\,\mathrm{K}$.

Sphere components:

Al_2O_3:

$$C_{\mathrm{m,Al_2O_3}} = \left[-55.82 + 0.7977\,\frac{T}{\mathrm{K}} - 0.00158\,\frac{T^2}{\mathrm{K^2}} + 1.669\cdot10^{-6}\,\frac{T^3}{\mathrm{K^3}} - 9.016\cdot10^{-10}\,\frac{T^4}{\mathrm{K^4}} + 1.966\cdot10^{-13}\,\frac{T^5}{\mathrm{K^5}}\right]\frac{\mathrm{J}}{\mathrm{mol\,K}} \tag{A.1}$$

CaO:

$$C_{\mathrm{m,CaO}} = \left[0.00425 + 0.2658\,\frac{T}{\mathrm{K}} - 5.871\cdot10^{-4}\,\frac{T^2}{\mathrm{K^2}} + 6.753\cdot10^{-7}\,\frac{T^3}{\mathrm{K^3}} - 3.896\cdot10^{-10}\,\frac{T^4}{\mathrm{K^4}} + 8.929\cdot10^{-14}\,\frac{T^5}{\mathrm{K^5}}\right]\frac{\mathrm{J}}{\mathrm{mol\,K}} \tag{A.2}$$

MgO:

$$C_{\mathrm{m,MgO}} = \left[-10.77 + 0.2956\,\frac{T}{\mathrm{K}} - 6.301\cdot10^{-4}\,\frac{T^2}{\mathrm{K^2}} + 7.056\cdot10^{-7}\,\frac{T^3}{\mathrm{K^3}} - 3.994\cdot10^{-10}\,\frac{T^4}{\mathrm{K^4}} + 9.026\cdot10^{-14}\,\frac{T^5}{\mathrm{K^5}}\right]\frac{\mathrm{J}}{\mathrm{mol\,K}} \tag{A.3}$$

SiO_2:
$T \leq 847\,\mathrm{K}$:

$$C_{\mathrm{m,SiO_2}} = \left[-5.230 + 0.2440\,\frac{T}{\mathrm{K}} - 2.966\cdot10^{-4}\,\frac{T^2}{\mathrm{K^2}} + 1.178\cdot10^{-7}\,\frac{T^3}{\mathrm{K^3}} + 4.467\cdot10^{-11}\,\frac{T^4}{\mathrm{K^4}} - 1.536\cdot10^{-14}\,\frac{T^5}{\mathrm{K^5}}\right]\frac{\mathrm{J}}{\mathrm{mol\,K}} \tag{A.4}$$

$847\,\mathrm{K} < T \leq 1079\,\mathrm{K}$:

$$C_{\mathrm{m,SiO_2}} = \left[58.78 + 0.01049\,\frac{T}{\mathrm{K}} - 5.133\cdot10^{-7}\,\frac{T^2}{\mathrm{K^2}} + 1.923\cdot10^{-10}\,\frac{T^3}{\mathrm{K^3}}\right]\frac{\mathrm{J}}{\mathrm{mol\,K}} \tag{A.5}$$

$1079\,\mathrm{K} < T \leq 1250\,\mathrm{K}$:

$$C_{\mathrm{m,SiO_2}} = \left[52.83 + 0.02508\,\frac{T}{\mathrm{K}} - 7.969\cdot10^{-6}\,\frac{T^2}{\mathrm{K^2}}\right]\frac{\mathrm{J}}{\mathrm{mol\,K}} \tag{A.6}$$

Particle components:

ZrO_2:

$$C_{\mathrm{m,ZrO_2}} = \left[-19.90 + 0.4865 \frac{T}{\mathrm{K}} - 0.0011 \frac{T^2}{\mathrm{K}^2} + 1.278 \cdot 10^{-6} \frac{T^3}{\mathrm{K}^3} - 7.442 \cdot 10^{-10} \frac{T^4}{\mathrm{K}^4} + 1.717 \cdot 10^{-13} \frac{T^5}{\mathrm{K}^5} \right] \frac{\mathrm{J}}{\mathrm{mol\,K}} \tag{A.7}$$

CeO_2:

$$C_{\mathrm{m,CeO_2}} = \left[6.392 + 0.3502 \frac{T}{\mathrm{K}} - 7.805 \cdot 10^{-4} \frac{T^2}{\mathrm{K}^2} + 9.099 \cdot 10^{-7} \frac{T^3}{\mathrm{K}^3} - 5.298 \cdot 10^{-10} \frac{T^4}{\mathrm{K}^4} + 1.222 \cdot 10^{-13} \frac{T^5}{\mathrm{K}^5} \right] \frac{\mathrm{J}}{\mathrm{mol\,K}} \tag{A.8}$$

B Sensitivity Coefficients

As equation 5.11 contains absolute values a distinction of cases has to be made. The equations for the sensitivity coefficients given below are valid only for $T_{\mathrm{S,in}} > T_{\mathrm{P,in}}$.

$$\begin{aligned}\frac{\partial \alpha}{\partial T_{\mathrm{P,in}}} =& -\frac{d_{\mathrm{S}}\,\rho_{\mathrm{S}}\left[c_{\mathrm{p,P}}\,m_{\mathrm{p,P}}\left(T_{\mathrm{P,out}}-T_{\mathrm{P,in}}\right)+c_{\mathrm{p,S}}\,m_{\mathrm{p,S}}\left(T_{\mathrm{S,in}}-T_{\mathrm{S,out}}\right)\right]}{12\,m_{\mathrm{S}}\,\tau\left(T_{\mathrm{S,in}}-T_{\mathrm{P,in}}\right)\cdot\left(-T_{\mathrm{P,in}}-T_{\mathrm{S,out}}+T_{\mathrm{P,out}}+T_{\mathrm{S,in}}\right)} \\ &- \frac{d_{\mathrm{S}}\,\rho_{\mathrm{S}}\,c_{\mathrm{p,P}}\,m_{\mathrm{P}}\ln\left(\frac{T_{\mathrm{S,in}}-T_{\mathrm{P,in}}}{T_{\mathrm{S,out}}-T_{\mathrm{P,out}}}\right)}{12\,m_{\mathrm{S}}\,\tau\left(-T_{\mathrm{P,in}}-T_{\mathrm{S,out}}+T_{\mathrm{P,out}}+T_{\mathrm{S,in}}\right)} \\ &+ \frac{d_{\mathrm{S}}\,\rho_{\mathrm{S}}\cdot\ln\left(\frac{T_{\mathrm{S,in}}-T_{\mathrm{P,in}}}{T_{\mathrm{S,out}}-T_{\mathrm{P,out}}}\right)\cdot\left[c_{\mathrm{p,P}}\,m_{\mathrm{p,P}}\left(T_{\mathrm{P,out}}-T_{\mathrm{P,in}}\right)+c_{\mathrm{p,S}}\,m_{\mathrm{p,S}}\left(T_{\mathrm{S,in}}-T_{\mathrm{S,out}}\right)\right]}{12\,m_{\mathrm{S}}\,\tau\left(-T_{\mathrm{P,in}}-T_{\mathrm{S,out}}+T_{\mathrm{P,out}}+T_{\mathrm{S,in}}\right)^{2}}\end{aligned} \tag{B.1}$$

$$\begin{aligned}\frac{\partial \alpha}{\partial T_{\mathrm{S,in}}} =& \frac{d_{\mathrm{S}}\,\rho_{\mathrm{S}}\left[c_{\mathrm{p,P}}\,m_{\mathrm{p,P}}\left(T_{\mathrm{P,out}}-T_{\mathrm{P,in}}\right)+c_{\mathrm{p,S}}\,m_{\mathrm{p,S}}\left(T_{\mathrm{S,in}}-T_{\mathrm{S,out}}\right)\right]}{12\,m_{\mathrm{S}}\,\tau\left(T_{\mathrm{S,in}}-T_{\mathrm{P,in}}\right)\cdot\left(-T_{\mathrm{P,in}}-T_{\mathrm{S,out}}+T_{\mathrm{P,out}}+T_{\mathrm{S,in}}\right)} \\ &+ \frac{d_{\mathrm{S}}\,\rho_{\mathrm{S}}\,c_{\mathrm{p,S}}\ln\left(\frac{T_{\mathrm{S,in}}-T_{\mathrm{P,in}}}{T_{\mathrm{S,out}}-T_{\mathrm{P,out}}}\right)}{12\,\tau\left(-T_{\mathrm{P,in}}-T_{\mathrm{S,out}}+T_{\mathrm{P,out}}+T_{\mathrm{S,in}}\right)} \\ &- \frac{d_{\mathrm{S}}\,\rho_{\mathrm{S}}\cdot\ln\left(\frac{T_{\mathrm{S,in}}-T_{\mathrm{P,in}}}{T_{\mathrm{S,out}}-T_{\mathrm{P,out}}}\right)\cdot\left[c_{\mathrm{p,P}}\,m_{\mathrm{p,P}}\left(T_{\mathrm{P,out}}-T_{\mathrm{P,in}}\right)+c_{\mathrm{p,S}}\,m_{\mathrm{p,S}}\left(T_{\mathrm{S,in}}-T_{\mathrm{S,out}}\right)\right]}{12\,m_{\mathrm{S}}\,\tau\left(-T_{\mathrm{P,in}}-T_{\mathrm{S,out}}+T_{\mathrm{P,out}}+T_{\mathrm{S,in}}\right)^{2}}\end{aligned} \tag{B.2}$$

$$\begin{aligned}\frac{\partial \alpha}{\partial T_{\mathrm{P,out}}} =& \frac{d_{\mathrm{S}}\,\rho_{\mathrm{S}}\left[c_{\mathrm{p,P}}\,m_{\mathrm{p,P}}\left(T_{\mathrm{P,out}}-T_{\mathrm{P,in}}\right)+c_{\mathrm{p,S}}\,m_{\mathrm{p,S}}\left(T_{\mathrm{S,in}}-T_{\mathrm{S,out}}\right)\right]}{12\,m_{\mathrm{S}}\,\tau\left(T_{\mathrm{S,out}}-T_{\mathrm{P,out}}\right)\cdot\left(-T_{\mathrm{P,in}}-T_{\mathrm{S,out}}+T_{\mathrm{P,out}}+T_{\mathrm{S,in}}\right)} \\ &+ \frac{d_{\mathrm{S}}\,\rho_{\mathrm{S}}\,c_{\mathrm{p,P}}\,m_{\mathrm{P}}\ln\left(\frac{T_{\mathrm{S,in}}-T_{\mathrm{P,in}}}{T_{\mathrm{S,out}}-T_{\mathrm{P,out}}}\right)}{12\,m_{\mathrm{S}}\,\tau\left(-T_{\mathrm{P,in}}-T_{\mathrm{S,out}}+T_{\mathrm{P,out}}+T_{\mathrm{S,in}}\right)} \\ &- \frac{d_{\mathrm{S}}\,\rho_{\mathrm{S}}\cdot\ln\left(\frac{T_{\mathrm{S,in}}-T_{\mathrm{P,in}}}{T_{\mathrm{S,out}}-T_{\mathrm{P,out}}}\right)\cdot\left[c_{\mathrm{p,P}}\,m_{\mathrm{p,P}}\left(T_{\mathrm{P,out}}-T_{\mathrm{P,in}}\right)+c_{\mathrm{p,S}}\,m_{\mathrm{p,S}}\left(T_{\mathrm{S,in}}-T_{\mathrm{S,out}}\right)\right]}{12\,m_{\mathrm{S}}\,\tau\left(-T_{\mathrm{P,in}}-T_{\mathrm{S,out}}+T_{\mathrm{P,out}}+T_{\mathrm{S,in}}\right)^{2}}\end{aligned} \tag{B.3}$$

$$\begin{aligned}\frac{\partial \alpha}{\partial T_{\mathrm{S,out}}} =& -\frac{d_{\mathrm{S}}\,\rho_{\mathrm{S}}\left[c_{\mathrm{p,P}}\,m_{\mathrm{p,P}}\left(T_{\mathrm{P,out}}-T_{\mathrm{P,in}}\right)+c_{\mathrm{p,S}}\,m_{\mathrm{p,S}}\left(T_{\mathrm{S,in}}-T_{\mathrm{S,out}}\right)\right]}{12\,m_{\mathrm{S}}\,\tau\left(T_{\mathrm{S,out}}-T_{\mathrm{P,out}}\right)\cdot\left(-T_{\mathrm{P,in}}-T_{\mathrm{S,out}}+T_{\mathrm{P,out}}+T_{\mathrm{S,in}}\right)} \\ &- \frac{d_{\mathrm{S}}\,\rho_{\mathrm{S}}\,c_{\mathrm{p,S}}\ln\left(\frac{T_{\mathrm{S,in}}-T_{\mathrm{P,in}}}{T_{\mathrm{S,out}}-T_{\mathrm{P,out}}}\right)}{12\,\tau\left(-T_{\mathrm{P,in}}-T_{\mathrm{S,out}}+T_{\mathrm{P,out}}+T_{\mathrm{S,in}}\right)} \\ &+ \frac{d_{\mathrm{S}}\,\rho_{\mathrm{S}}\cdot\ln\left(\frac{T_{\mathrm{S,in}}-T_{\mathrm{P,in}}}{T_{\mathrm{S,out}}-T_{\mathrm{P,out}}}\right)\cdot\left[c_{\mathrm{p,P}}\,m_{\mathrm{p,P}}\left(T_{\mathrm{P,out}}-T_{\mathrm{P,in}}\right)+c_{\mathrm{p,S}}\,m_{\mathrm{p,S}}\left(T_{\mathrm{S,in}}-T_{\mathrm{S,out}}\right)\right]}{12\,m_{\mathrm{S}}\,\tau\left(-T_{\mathrm{P,in}}-T_{\mathrm{S,out}}+T_{\mathrm{P,out}}+T_{\mathrm{S,in}}\right)^{2}}\end{aligned} \tag{B.4}$$

$$\frac{\partial \alpha}{\partial m_{\mathrm{P}}} = \frac{d_{\mathrm{S}}\,\rho_{\mathrm{S}}\,c_{\mathrm{p,P}}\ln\left(\frac{T_{\mathrm{S,in}}-T_{\mathrm{P,in}}}{T_{\mathrm{S,out}}-T_{\mathrm{P,out}}}\right)\cdot\left(T_{\mathrm{P,out}}-T_{\mathrm{P,in}}\right)}{12\,m_{\mathrm{S}}\,\tau\left(-T_{\mathrm{P,in}}-T_{\mathrm{S,out}}+T_{\mathrm{P,out}}+T_{\mathrm{S,in}}\right)} \tag{B.5}$$

$$\frac{\partial \alpha}{\partial m_{\mathrm{S}}} = -\frac{d_{\mathrm{S}}\,\rho_{\mathrm{S}}\,c_{\mathrm{p,P}}\,m_{\mathrm{P}}\ln\left(\frac{T_{\mathrm{S,in}}-T_{\mathrm{P,in}}}{T_{\mathrm{S,out}}-T_{\mathrm{P,out}}}\right)\cdot\left(T_{\mathrm{P,out}}-T_{\mathrm{P,in}}\right)}{12\,m_{\mathrm{S}}^{2}\,\tau\left(-T_{\mathrm{P,in}}-T_{\mathrm{S,out}}+T_{\mathrm{P,out}}+T_{\mathrm{S,in}}\right)} \tag{B.6}$$

$$\frac{\partial \alpha}{\partial c_{\mathrm{p,P}}} = \frac{d_{\mathrm{S}}\,\rho_{\mathrm{S}}\,m_{\mathrm{P}}\ln\left(\frac{T_{\mathrm{S,in}}-T_{\mathrm{P,in}}}{T_{\mathrm{S,out}}-T_{\mathrm{P,out}}}\right)\cdot\left(T_{\mathrm{P,out}}-T_{\mathrm{P,in}}\right)}{12\,m_{\mathrm{S}}\,\tau\left(-T_{\mathrm{P,in}}-T_{\mathrm{S,out}}+T_{\mathrm{P,out}}+T_{\mathrm{S,in}}\right)} \tag{B.7}$$

$$\frac{\partial \alpha}{\partial c_{\mathrm{p,S}}} = \frac{d_{\mathrm{S}}\,\rho_{\mathrm{S}}\ln\left(\frac{T_{\mathrm{S,in}}-T_{\mathrm{P,in}}}{T_{\mathrm{S,out}}-T_{\mathrm{P,out}}}\right)\cdot\left(T_{\mathrm{S,out}}-T_{\mathrm{S,in}}\right)}{12\,\tau\left(-T_{\mathrm{P,in}}-T_{\mathrm{S,out}}+T_{\mathrm{P,out}}+T_{\mathrm{S,in}}\right)} \tag{B.8}$$

$$\frac{\partial \alpha}{\partial d_{\mathrm{S}}} = \frac{\rho_{\mathrm{S}}\ln\left(\frac{T_{\mathrm{S,in}}-T_{\mathrm{P,in}}}{T_{\mathrm{S,out}}-T_{\mathrm{P,out}}}\right)\cdot\left[c_{\mathrm{p,P}}\,m_{\mathrm{p,P}}\left(T_{\mathrm{P,out}}-T_{\mathrm{P,in}}\right)+c_{\mathrm{p,S}}\,m_{\mathrm{p,S}}\left(T_{\mathrm{S,in}}-T_{\mathrm{S,out}}\right)\right]}{12\,m_{\mathrm{S}}\,\tau\left(-T_{\mathrm{P,in}}-T_{\mathrm{S,out}}+T_{\mathrm{P,out}}+T_{\mathrm{S,in}}\right)} \tag{B.9}$$

$$\frac{\partial \alpha}{\partial \rho_{\mathrm{S}}} = \frac{d_{\mathrm{S}}\ln\left(\frac{T_{\mathrm{S,in}}-T_{\mathrm{P,in}}}{T_{\mathrm{S,out}}-T_{\mathrm{P,out}}}\right)\cdot\left[c_{\mathrm{p,P}}\,m_{\mathrm{p,P}}\left(T_{\mathrm{P,out}}-T_{\mathrm{P,in}}\right)+c_{\mathrm{p,S}}\,m_{\mathrm{p,S}}\left(T_{\mathrm{S,in}}-T_{\mathrm{S,out}}\right)\right]}{12\,m_{\mathrm{S}}\,\tau\left(-T_{\mathrm{P,in}}-T_{\mathrm{S,out}}+T_{\mathrm{P,out}}+T_{\mathrm{S,in}}\right)} \tag{B.10}$$

$$\frac{\partial \alpha}{\partial \tau} = -\frac{d_{\mathrm{S}}\,\rho_{\mathrm{S}}\ln\left(\frac{T_{\mathrm{S,in}}-T_{\mathrm{P,in}}}{T_{\mathrm{S,out}}-T_{\mathrm{P,out}}}\right)\cdot\left[c_{\mathrm{p,P}}\,m_{\mathrm{p,P}}\left(T_{\mathrm{P,out}}-T_{\mathrm{P,in}}\right)+c_{\mathrm{p,S}}\,m_{\mathrm{p,S}}\left(T_{\mathrm{S,in}}-T_{\mathrm{S,out}}\right)\right]}{12\,m_{\mathrm{S}}\,\tau^{2}\left(-T_{\mathrm{P,in}}-T_{\mathrm{S,out}}+T_{\mathrm{P,out}}+T_{\mathrm{S,in}}\right)} \tag{B.11}$$